nature cell biology

ARTICLES

https://doi.org/10.1038/s41556-018-0256-3

Chemotherapy elicits pro-metastatic extracellular vesicles in breast cancer models

Ioanna Keklikoglou[1,10*], Chiara Cianciaruso[1,10], Esra Güç[2], Mario Leonardo Squadrito[1], Laura M. Spring[3], Simon Tazzyman[4], Lore Lambein[4], Amanda Poissonnier[5], Gino B. Ferraro[6], Caroline Baer[1], Antonino Cassará[1], Alan Guichard[1], M. Luisa Iruela-Arispe[1,7], Claire E. Lewis[4], Lisa M. Coussens[5,8], Aditya Bardia[3], Rakesh K. Jain[6], Jeffrey W. Pollard[2,9] and Michele De Palma[1*]

Cytotoxic chemotherapy is an effective treatment for invasive breast cancer. However, experimental studies in mice also suggest that chemotherapy has pro-metastatic effects. Primary tumours release extracellular vesicles (EVs), including exosomes, that can facilitate the seeding and growth of metastatic cancer cells in distant organs, but the effects of chemotherapy on tumour-derived EVs remain unclear. Here we show that two classes of cytotoxic drugs broadly employed in pre-operative (neoadjuvant) breast cancer therapy, taxanes and anthracyclines, elicit tumour-derived EVs with enhanced pro-metastatic capacity. Chemotherapy-elicited EVs are enriched in annexin A6 (ANXA6), a Ca^{2+}-dependent protein that promotes NF-κB-dependent endothelial cell activation, *Ccl2* induction and $Ly6C^{+}CCR2^{+}$ monocyte expansion in the pulmonary pre-metastatic niche to facilitate the establishment of lung metastasis. Genetic inactivation of *Anxa6* in cancer cells or *Ccr2* in host cells blunts the pro-metastatic effects of chemotherapy-elicited EVs. ANXA6 is detected, and potentially enriched, in the circulating EVs of breast cancer patients undergoing neoadjuvant chemotherapy.

Neoadjuvant chemotherapy provides long-term clinical benefits to patients diagnosed with invasive breast cancer, especially when the primary tumour fully regresses before surgery[1–6]. However, the therapeutic benefits of neoadjuvant chemotherapy may be limited by tumour-promoting host responses that are induced by certain cytotoxic drugs[7]. Several reports have documented pro-metastatic effects of cytotoxic agents in mouse mammary tumour models[8–13]. For example, paclitaxel (PTX), a microtubule-stabilizing drug that is often used in breast cancer therapy[5,6], was reported to enhance the expression of vascular-endothelial growth factor receptor-1 on pulmonary endothelial cells to facilitate cancer-cell adhesion and subsequent metastasis[13]. Both PTX and doxorubicin (DOX)—an anthracycline also used in breast cancer therapy[5,6]—increased the ability of perivascular $TIE2^{+}$ macrophages[14–16] to promote cancer-cell intravasation in primary mammary tumours, thus resulting in heightened pulmonary metastasis[8,12]. Collectively, pre-clinical data in mouse models suggest that the pro-metastatic capacity of certain chemotherapies may involve the facilitation of both cancer cell intravasation in primary tumours and extravasation to secondary, metastatic sites.

Primary tumours release extracellular vesicles (EVs) that can modulate the biology of distant organ niches to enhance seeding and growth of metastatic cancer cells[17–24]. In this study, we examined the effects of PTX and DOX on the release, properties and pro-metastatic potential of tumour-derived EVs in mouse models of chemoresistant breast cancer.

Results

PTX enhances pulmonary metastasis in mouse mammary tumour models. We examined the effects of PTX on metastasis in two mouse breast cancer models: transgenic MMTV-PyMT mice (FVB/n background) that develop multifocal mammary tumours[25–27] and immunodeficient *Rag1*$^{-/-}$ (C57BL/6 background) or Swiss nu/nu mice challenged with 4T1 cancer cells[28]. To trace metastasis, the 4T1 cells were modified to express a fluorescent CD9–mCherry (mCh) fusion protein targeted to cellular membranes; in some experiments, 4T1 cells were further modified to express a human *ERBB2* (HER2) transgene[29]. The 4T1 tumour studies used immunodeficient mice to avoid potential anti-tumour immune responses against mCh or HER2.

Tumour-bearing mice received three doses of PTX (10 mg kg^{-1}) or vehicle (cremophor EL; CREMO) before analysis (Fig. 1a). Treatment with PTX had modest, if any, inhibitory activity on the growth of primary mammary tumours in both the MMTV-PyMT and 4T1 models (Fig. 1b–e). However, it resulted in increased pulmonary tumour deposits in a fraction of the mice, in line with previous findings[8–12]. In particular, PTX increased the incidence (Fig. 1f,g) and mean size (Fig. 1f,h,i) of spontaneous metastases in the lungs of MMTV-PyMT mice, as well as the seeding of mCh^{+} 4T1 cancer cells in the lungs of tumour-bearing *Rag1*$^{-/-}$ mice (Fig. 1j,k) compared with vehicle. It also enhanced pulmonary seeding of $mCh^{+}HER2^{+}$ cancer cells in some tumour-bearing Swiss nu/nu mice (Fig. 1l), although it did not augment the frequency of $mCh^{+}HER2^{+}$ cancer

[1]Swiss Institute for Experimental Cancer Research (ISREC), School of Life Sciences, École Polytechnique Fédérale de Lausanne (EPFL), Lausanne, Switzerland. [2]MRC Centre for Reproductive Health, Queen's Medical Research Institute, The University of Edinburgh, Edinburgh, UK. [3]Massachusetts General Hospital Cancer Center, Harvard Medical School, Boston, MA, USA. [4]Department of Oncology and Metabolism, Medical School, University of Sheffield, Sheffield, UK. [5]Department of Cell, Developmental and Cancer Biology, Oregon Health and Sciences University, Portland, OR, USA. [6]Edwin L. Steele Laboratories, Department of Radiation Oncology, Harvard Medical School, Massachusetts General Hospital, Boston, MA, USA. [7]Department of Molecular Cell and Developmental Biology, Molecular Biology Institute, Jonsson Comprehensive Cancer Center, University of California Los Angeles, Los Angeles, CA, USA. [8]Knight Cancer Institute, Oregon Health and Science University, Portland, OR, USA. [9]Department of Developmental and Molecular Biology, Albert Einstein College of Medicine, New York, NY, USA. [10]These authors contributed equally: Ioanna Keklikoglou, Chiara Cianciaruso. *e-mail: ioanna.keklikoglou@epfl.ch; michele.depalma@epfl.ch

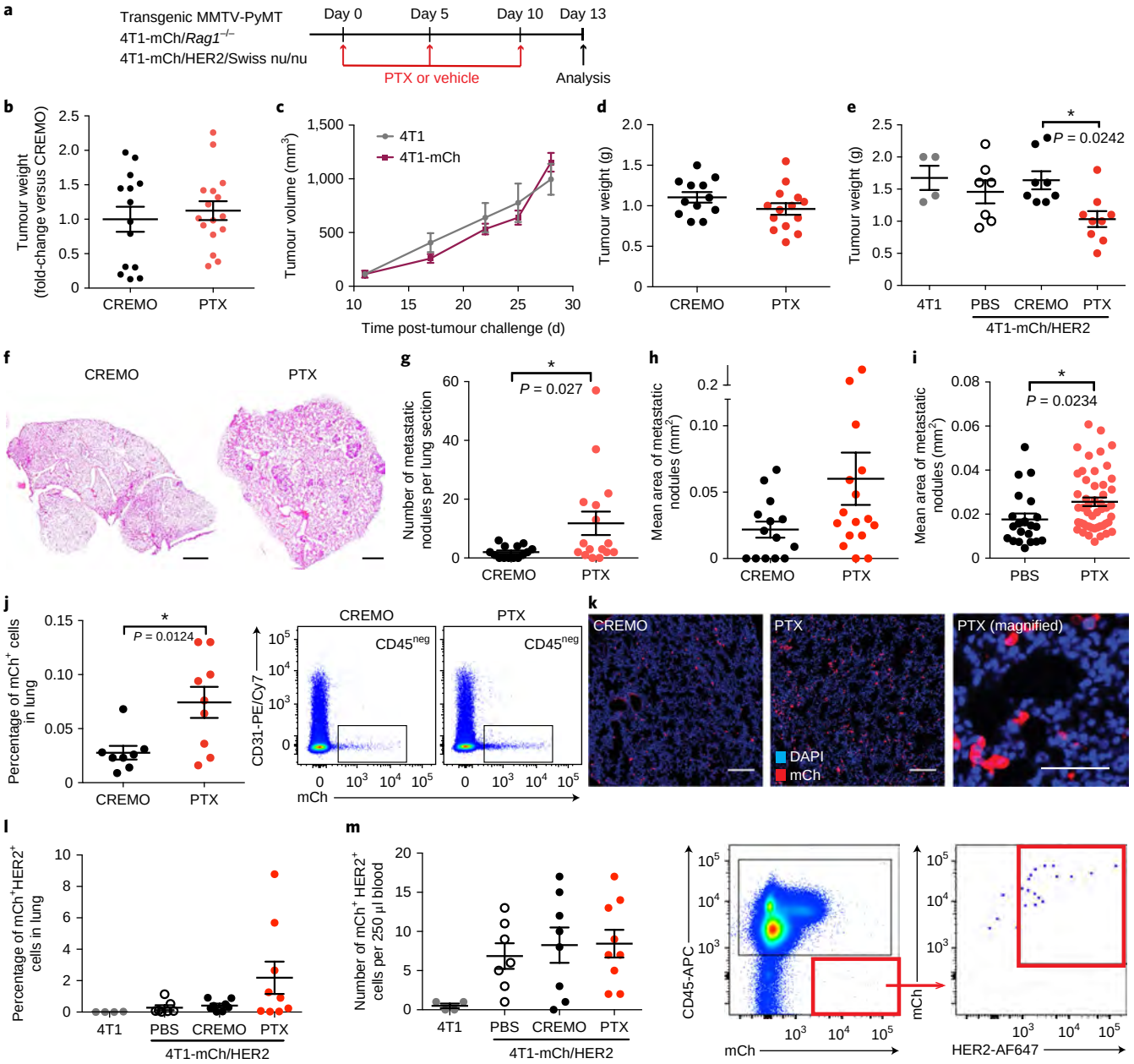

Fig. 1 | PTX enhances pulmonary metastasis in mammary tumour-bearing mice. a, Drug scheduling in tumour-bearing mice. **b**, Cumulative weight of multifocal mammary tumours (mean ± s.e.m.) in MMTV-PyMT mice. CREMO, $n = 14$ mice; PTX, $n = 16$ mice. Each dot represents one mouse carrying several tumours. Data show two independent experiments combined (EPFL cohort). **c**, Volume of 4T1 and 4T1-mCh tumours in untreated *Rag1*$^{-/-}$ mice (mean ± s.e.m.; $n = 7$ mice per group). **d**, Weight and 4T1-mCh tumours in *Rag1*$^{-/-}$ mice (mean ± s.e.m.). CREMO, $n = 12$ mice; PTX, $n = 14$ mice. Data show two independent experiments combined. **e**, Weight of 4T1 ($n = 4$) and 4T1-mCh/HER2 tumours (mean ± s.e.m.) in Swiss nu/nu mice. $n = 7$, 8 and 9 mice for the PBS, CREMO and PTX 4T1-mCh/HER2 groups, respectively. The statistical analyses were performed using one-way ANOVA with Tukey's multiple comparison tests. **f**, Representative H&E images of lung sections of MMTV-PyMT mice from the experiment shown in **b**. Scale bars, 1 mm. The data are quantified in **g** and **h**. **g–i**, The number (**g**) and mean area (**h**,**i**) of pulmonary metastases (mean ± s.e.m.) in MMTV-PyMT mice. **g**,**h**, CREMO, $n = 14$ mice; PTX, $n = 16$ mice; two independent experiments combined (EPFL cohort). **i**, PBS, $n = 21$; PTX, $n = 49$; five independent experiments combined (OHSU cohort). The statistical analyses in **g** and **i** were performed using unpaired two-tailed Student's *t*-tests. **j**, FACS analysis of mCh$^+$CD31$^-$ cancer cells (relative to viable CD45$^-$ lung-derived cells; mean ± s.e.m.) in the lungs of 4T1-mCh tumour-bearing mice. CREMO, $n = 8$ mice; PTX, $n = 9$ mice. Statistical analysis was performed as in **g**. The FACS panels on the right show the gating strategy employed. **k**, Representative confocal immunofluorescence images showing mCh$^+$ 4T1 cancer cells in lung sections of mice from the experiment in **j**. The nuclei are stained with DAPI. Scale bars, 200 µm (left and middle) and 50 µm (right). **l**, FACS analysis of mCh$^+$CD31$^-$ cancer cells (mean ± s.e.m.) in the lungs of 4T1 ($n = 4$) or 4T1-mCh/HER2 tumour-bearing mice. $n = 7$, 8 and 9 mice for the PBS, CREMO and PTX 4T1-mCh/HER2 groups, respectively. **m**, FACS analysis of mCh$^+$HER2$^+$CD45$^-$ cancer cells (mean ± s.e.m.; absolute cell counts) in the blood of 4T1 ($n = 4$) or 4T1-mCh/HER2 tumour-bearing mice. $n = 7$, 8 and 9 mice for the PBS, CREMO and PTX 4T1-mCh/HER2 groups, respectively. The FACS panels on the right show the gating strategy employed. The source data are shown in Supplementary Table 5.

cells in the systemic circulation (Fig. 1m). Together, these results indicate that PTX may augment, rather than limit, lung metastasis in mouse models of chemoresistant breast cancer.

Chemotherapy-elicited EVs promote mammary tumour metastasis in mice. Tumour-derived EVs facilitate metastasis of primary tumours by altering the properties of pre-metastatic niche-associated host cells[17–24]. To gauge the participation of tumour-derived EVs in PTX-induced mammary tumour metastasis, we used sequential ultracentrifugation to isolate EVs[30,31] from the cell culture media of unmodified 4T1 cancer cells that were treated with either PTX or CREMO (PTX-EV and CREMO-EV, respectively). The resulting preparations were highly enriched in small EVs, as shown by both transmission electron microscopy (TEM; Fig. 2a) and nanoparticle tracking analysis (NTA; Supplementary Fig. 1a). In addition, the EV-associated proteins CD9, CD81 and syntenin-1 were enriched in EVs compared with producer cells as demonstrated by western blot analysis (Supplementary Fig. 1b). Although we cannot rule out co-purification of small apoptotic bodies, the physical and molecular properties of the preparations are consistent with bona fide EVs[30–32] with a mode size between 100 and 150 nm.

We pre-conditioned immunocompetent Balb/c mice with either PTX-EV or CREMO-EV (two doses corresponding to about 4×10^9 EVs each; Supplementary Fig. 1c) followed by intravenous injection of 4T1 cells (Fig. 2b). In this lung colonization assay, PTX-EV increased the number of metastatic lung nodules compared with CREMO-EV (Fig. 2c). We then investigated whether PTX could also affect the pro-metastatic capacity of EVs that were released from an intact tumour microenvironment. To this aim, we treated MMTV-PyMT mice with either PTX or CREMO (Fig. 1a), excised mammary tumours three days after the last dose and cultured tumour-derived cell suspensions for 48 h to isolate EVs from conditioned media (Fig. 2d). We assessed the purity and properties of EV preparations by TEM (Supplementary Fig. 1d), NTA (Supplementary Fig. 1e,f) and western blot analysis (Supplementary Fig. 1g) and found no obvious differences between PTX-EVs and CREMO-EVs. We then pre-conditioned immunocompetent FVB/n mice with either EV preparation (Fig. 2b) followed by the intravenous injection of freshly isolated MMTV-PyMT tumour-derived cells. Similar to the results obtained with 4T1 cells, PTX-EVs increased the number of metastatic nodules in this MMTV-PyMT-based lung colonization assay (Fig. 2e).

Anthracyclines are broadly employed in neoadjuvant breast cancer therapy[1,5,6]. DOX, a lead anthracycline, was previously reported to modify the microenvironment of primary mammary tumours thus potentially facilitating metastasis[8,33]. We treated MMTV-PyMT mice with DOX or vehicle (PBS) and purified tumour-derived DOX-EVs and PBS-EVs, respectively, according to the method shown in Fig. 2d. Similar to the results obtained with PTX-EV, DOX-EV enhanced metastasis compared with PBS-EV in an MMTV-PyMT-based lung colonization assay (Fig. 2f). Notably, neither PTX nor DOX directly increased metastasis in this assay; rather, the free drugs limited, or even abated, lung colonization by MMTV-PyMT tumour-derived cells (Fig. 2g). These results indicate that chemotherapy-elicited, tumour-derived EVs mediate the pro-metastatic activity of the cytotoxic drugs.

PTX-elicited EVs facilitate tumour colonization in a zebrafish embryo model. Because tumour-derived EVs cannot be isolated from mouse plasma in sufficient amounts to perform EV transfer experiments in mice, we examined the pro-metastatic capacity of circulating PTX-EVs in a zebrafish embryo model. In this system, cancer cells injected into the circulation extravasate to and colonize the caudal haematopoietic area (CHA) of the tail of embryos; these events can be imaged by confocal microscopy as the embryos are translucent[34,35]. We found that PTX-EVs isolated from the plasma of 4T1-mCh tumour-bearing *Rag1*$^{-/-}$ mice (Fig. 2h) enhanced CHA colonization by human MDA-MB-435 melanoma cells stably expressing cyan fluorescent protein (CFP) compared with CREMO-EV (Fig. 2i–l). Notably, free PTX did not facilitate CHA colonization by cancer cells in the same assay.

PTX modulates EV release from cancer cells. We then examined the effects of chemotherapy on the release of EVs from cancer cells. Treatment with PTX increased the release of EVs from both mouse and human mammary carcinoma cell lines (Supplementary Fig. 2a–c). It also increased mCh fluorescence in the blood of mice carrying 4T1-mCh tumours (Supplementary Fig. 2d–f). In these experiments, mCh fluorescence was associated with bona fide EVs (Supplementary Fig. 2g–i) and was resistant to proteolysis (Supplementary Fig. 2j,k), thus indicating intravesicular localization of the CD9–mCh fusion protein.

Cytotoxic agents, including PTX, promote cancer cell death in a dose-dependent manner (Supplementary Figs. 2a and 3a,b). Although drug-induced cell stress may influence the release of EVs and other microvesicles from pre-apoptotic cells[32], PTX-induced EV release from 4T1 cells was apoptosis-independent (Supplementary Fig. 3c).

Rab GTPases control the biogenesis and release of EVs in mammalian cells[36,37]. Accordingly, both basal and PTX-induced EV release were reduced in *Rab27a*-deficient 4T1 cells (Supplementary Fig. 3d–g). PTX may enhance the release of EVs from cancer cells by enforcing the trafficking of intracellular vesicles to plasma membranes (Supplementary Fig. 3h); this process may involve the association of RAB27A with microtubules that are stabilized by taxanes[38]. We also observed enhanced EV release from 4T1 cells that were exposed to a different taxane, docetaxel (Supplementary Fig. 3i). Conversely, DOX did not promote the release of EVs from mammary carcinoma cells (Supplementary Fig. 3j, k). Therefore, whereas taxanes may increase mammary tumour metastasis by enhancing both the release and pro-metastatic properties of tumour-derived EVs, anthracyclines may do so by specifically reinforcing the pro-metastatic features of the EVs.

Chemotherapy-elicited EVs are enriched in ANXA6. The enhanced pro-metastatic capacity of chemotherapy-elicited EVs may depend on their protein repertoire. We performed proteomic analysis of 4T1-derived PTX-EV and CREMO-EV using liquid chromatography–tandem mass spectrometry (LC–MS/MS). Unsupervised clustering analysis of the EV proteomes (Fig. 3a) revealed substantial differences (Supplementary Table 1). Over-represented proteins in PTX-EVs included annexin A6 (ANXA6; Fig. 3b), a Ca^{2+}-binding membrane-associated protein (Fig. 3c). ANXA6 controls membrane trafficking and cell signalling[39] and has been previously implicated in both the positive and negative regulation of cancer cell invasion[40–42]. Validation experiments by western blotting revealed that ANXA6 was more robustly detected in PTX-EV compared with the producer 4T1 cells or CREMO-EV (Fig. 3d). Notably, both PTX and DOX promoted ANXA6 loading into the EVs of 4T1 cells and the MMTV-PyMT tumour-derived cell line PyMT-IK1 (Fig. 3e).

Both taxanes[43] and anthracyclines[44] augment intracellular calcium ion levels. Interestingly, chemotherapy-induced ANXA6 loading into EVs was Ca^{2+}-dependent (Fig. 3f–i), whereas EV release per se was Ca^{2+} independent (Fig. 3j). Western blotting and density gradient fractionation of EVs[30] purified from medium conditioned by 4T1 or 4T1-mCh cells confirmed that ANXA6 was associated with bona fide EVs (Supplementary Figs. 1b and 4a,b) and, in particular, with the inner leaflet of EVs (Supplementary Fig. 4c,d). Neither PTX nor DOX increased ANXA6 in EVs released by non-transformed cells, such as mouse primary bone marrow dendritic cells and embryonic fibroblasts (Supplementary Fig. 4e–h).

EV-associated ANXA6 promotes mammary tumour metastasis. The aforementioned results suggested a potential role for ANXA6 in the modulation of chemotherapy-induced mammary

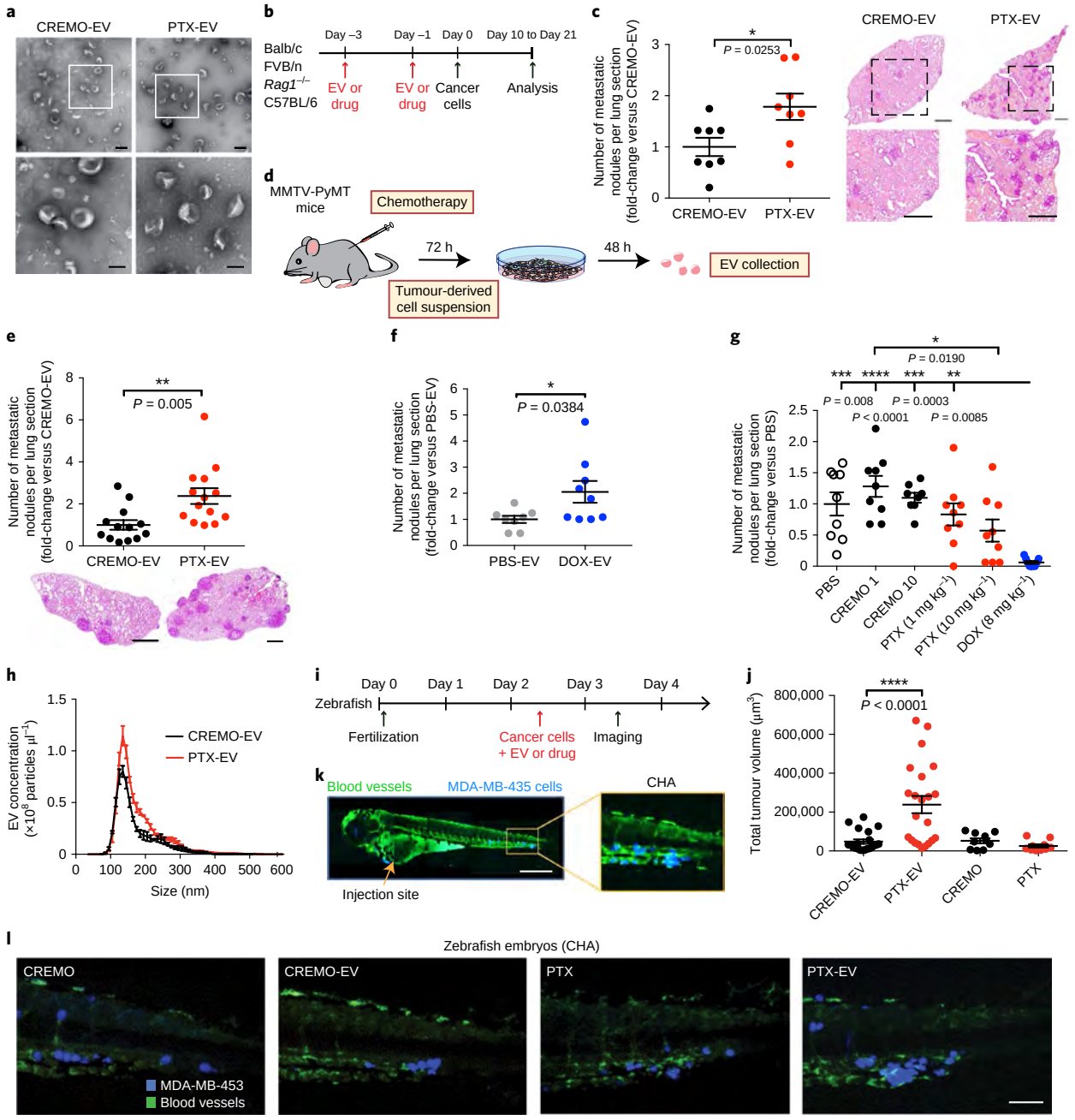

Fig. 2 | Chemotherapy-elicited EVs are pro-metastatic in mouse and zebrafish tumour models. a, TEM images of CREMO-EV ($n=1$ biological sample) and PTX-EV ($n=2$ independent biological samples) isolated from 4T1 cells. One representative image is shown for each EV type. The bottom panels show magnified fields of the white squares in the top panels. Scale bars, 200 nm (top) and 100 nm (bottom). **b**, Schematic illustrating the lung pre-conditioning and tumour colonization assays. **c**, Number of 4T1 metastatic nodules (mean ± s.e.m.; $n=8$ mice per group) in the lungs of pre-conditioned Balb/c mice. Statistical analysis was performed using an unpaired two-tailed Student's *t*-test. The right panels show representative H&E images of lung sections with magnified fields of the dashed boxes shown in the bottom panels. Scale bars, 1 mm. **d**, Procedure used to isolate tumour-derived EVs from chemotherapy-treated MMTV-PyMT mice. **e**,**f**, Number of MMTV-PyMT metastatic nodules (mean ± s.e.m.) in the lungs of pre-conditioned FVB/n mice. CREMO-EV, $n=13$; PTX-EV, $n=14$; PBS-EV, $n=8$ and DOX-EV, $n=9$ mice. The statistical analyses were performed as in **c**. The bottom panels in **e** show representative H&E images of lung sections. Scale bars, 1 mm. **g**, Number of MMTV-PyMT metastatic nodules (mean ± s.e.m.) in the lungs of FVB/n mice pre-conditioned with different drug regimens. $n=9$ mice for the PBS, CREMO 1, PTX (1 mg kg^{-1} and 10 mg kg^{-1}) and DOX groups, and $n=8$ mice for the CREMO 10 group. CREMO 1 and 10 are the vehicle controls for 1 and 10 mg kg^{-1} PTX, respectively. The statistical analyses were performed using one-way ANOVA with Tukey's multiple comparison tests. **h**, Concentration (mean ± s.e.m.; $n=5$ acquisitions of one sample per condition) and size distribution, calculated by NTA, of EVs that were isolated from the plasma of 4T1-mCh tumour-bearing mice treated as indicated. **i**, Schematic illustrating the experiments conducted on zebrafish embryos. **j**, Volume of CFP$^+$ MDA-MB-453 tumour deposits (mean ± s.e.m.) in zebrafish embryos injected with CREMO-EVs ($n=24$), PTX-EVs ($n=22$), CREMO ($n=12$) or PTX ($n=12$) as determined by confocal imaging analysis. Statistical analyses were conducted as in **g**. **k**, Confocal image of a representative zebrafish embryo injected with CFP$^+$ MDA-MB-453 cells. The blood vessels are GFP$^+$. The right panel shows the CHA with CFP$^+$ tumour deposits. Scale bar, 0.5 mm. **l**, Representative confocal images of the CHA of zebrafish embryos imaged as in **k**. Scale bar, 70 μm. The quantitative data are shown in **j**. The source data are shown in Supplementary Table 5.

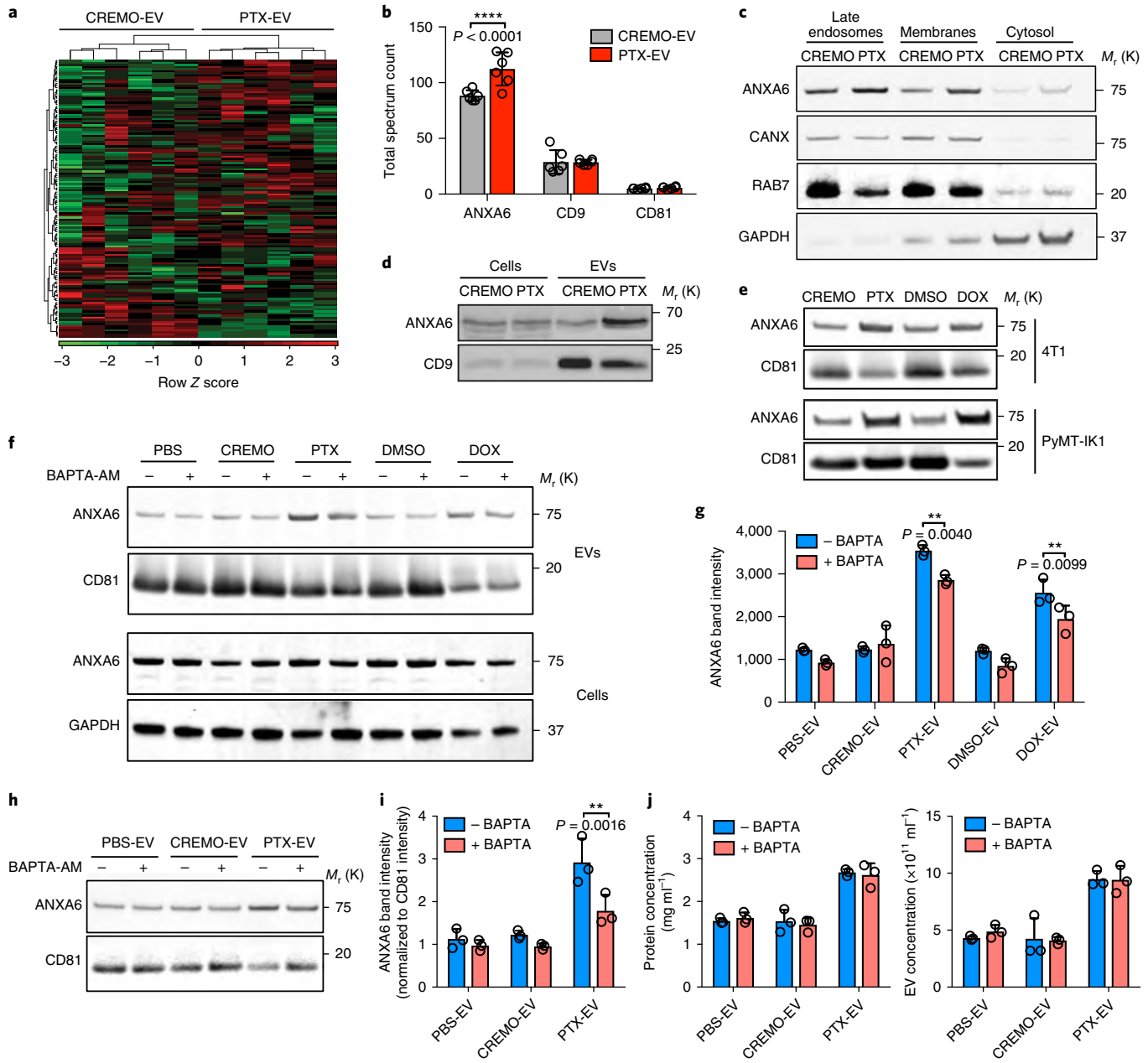

Fig. 3 | PTX enriches ANXA6 in EVs in a Ca^{2+}-dependent manner. a, Unsupervised clustering of proteins in CREMO-EV and PTX-EV ($n = 6$ independent EV preparations per condition) from 4T1 cells as determined by LC–MS/MS analysis. **b**, LC–MS/MS analysis of CREMO-EV and PTX-EV ($n = 6$ independent EV preparations each) from 4T1 cells showing total spectrum count (mean ± s.d.) of ANXA6, CD9 and CD81. The statistical analyses were performed using two-way ANOVA with Sidak's multiple comparison tests. **c**, Western blot analysis of ANXA6, calnexin (CANX), glyceraldehyde 3-phosphate dehydrogenase (GAPDH) and ras-related protein Rab-7 (RAB7) in 4T1 cells treated with CREMO or PTX for 24 h before subcellular fractionation. The 'membranes' fraction encompasses the early and late endosomes, endoplasmic reticulum and mitochondria. The experiment was performed once. M_r (K), relative molecular weight (kilodaltons). **d**, Western blot analysis of ANXA6 and CD9 in CREMO- or PTX-treated 4T1 cells, or matched CREMO-EV or PTX-EV. Additional experiments are shown in **e**,**f**,**h**, Fig. 4c and Supplementary Fig. 1b. **e**, Western blot analysis of ANXA6 and CD81 in the indicated EV preparations isolated from either 4T1 (top) or PyMT-IK1 (bottom) cells. **f**, Western blot analysis of the indicated proteins in PyMT-IK1 cells (bottom) and matched EVs (top) 48 h after treatment of the cells with PBS, CREMO, PTX, dimethylsulfoxide (DMSO) or DOX, with or without the calcium chelator BAPTA-AM. One representative of the three experiments performed is shown for the EVs; one experiment was conducted for the cells. **g**, ANXA6 band intensity (mean ± s.d.; $n = 3$ independent experiments, one of which is shown in **f** above) in the indicated EV preparations from PyMT-IK1 cells analysed by western blotting. The statistical analyses were performed as in **b**. **h**, Western blot analysis of EVs from 4T1 cells treated for 48 h with PBS, CREMO or PTX, with or without BAPTA-AM. One representative experiment is shown of the three performed. **i**, ANXA6 band intensity (normalized to CD81; mean ± s.d.; $n = 3$ independent experiments, one of which is shown in **h**) in the indicated 4T1 EV preparations. The statistical analyses were performed as in **b**. **j**, Protein content as determined by BCA (left) and EV concentration, determined by NTA (right), of the indicated EV preparations (mean ± s.d.; $n = 3$ independent EV preparation per condition) obtained from 4T1 cells treated with or without BAPTA-AM. The statistical analyses were performed as in **b**. The source data are shown in Supplementary Table 5. Unprocessed blots are shown in Supplementary Fig. 9.

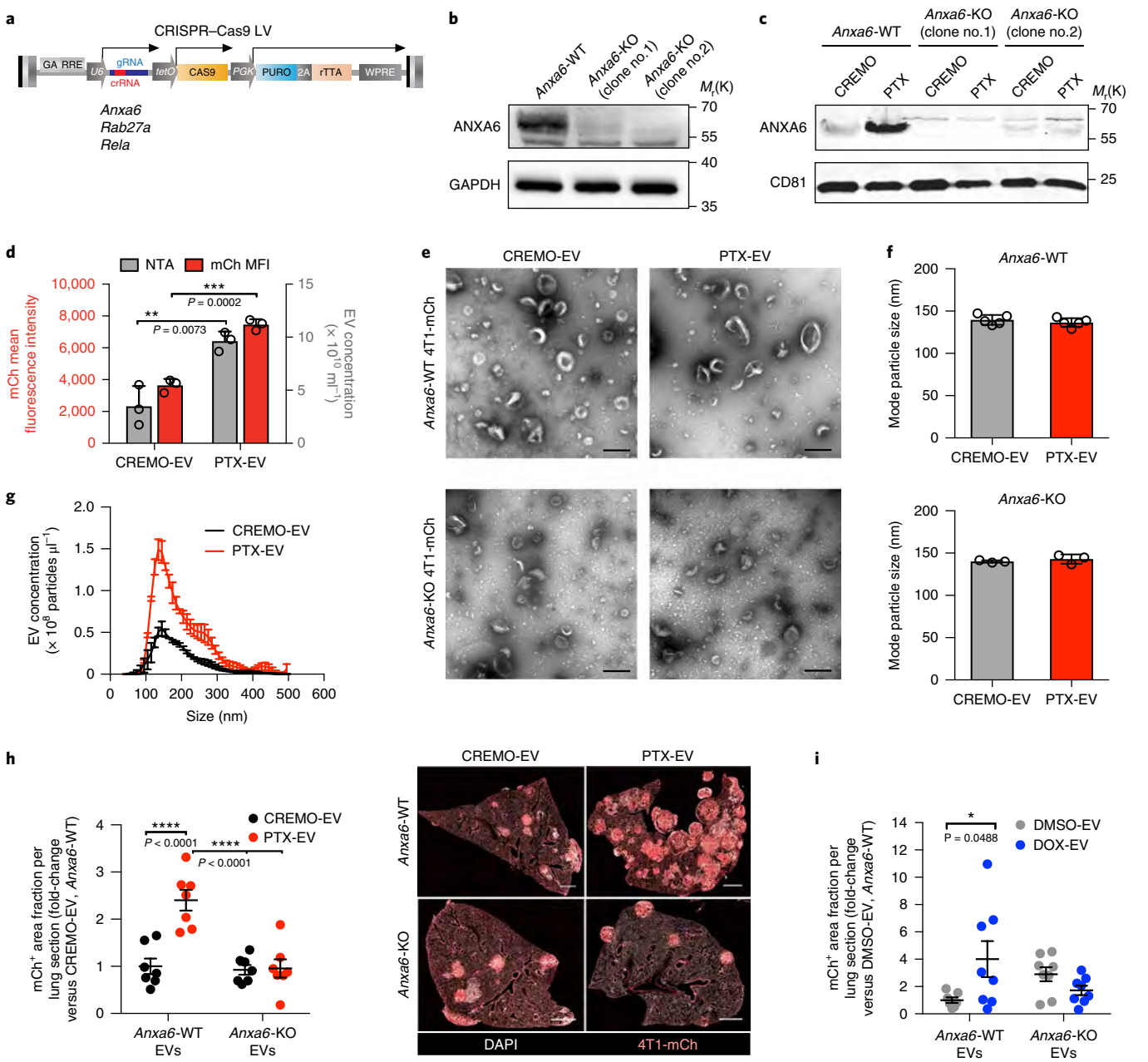

Fig. 4 | EV-associated ANXA6 promotes mammary tumour metastasis. a, Schematic of the lentiviral vectors used to disrupt the expression of *Anxa6*, *Rab27a* or *Rela* in cells. gRNA, guide RNA; crRNA, CRISPR RNA. **b**,**c**, Western blot analysis of ANXA6, GAPDH and CD81 in 4T1-mCh cells (**b**) or secreted EVs (**c**). *Anxa6*-WT (parental line) and two independent *Anxa6*-KO clones are shown, either untreated (**b**) or treated as indicated (**c**). The experiments were performed once. **d**, Mean fluorescence intensity of mCh (left *y* axis) and EV concentration, determined by NTA (right *y* axis), of EVs (mean ± s.d.; $n = 3$ independent cell cultures per condition) released by *Anxa6*-KO 4T1-mCh cells (clone no. 1) treated for 72 h with either CREMO or PTX. The statistical analyses were performed using unpaired two-tailed Student's *t*-tests. **e**, Representative wide-field TEM images of the indicated EVs isolated from *Anxa6*-WT (top) or *Anxa6*-KO (clone no. 1; bottom) 4T1-mCh cells. Scale bars, 200 nm. The experiment was performed once. **f**, Mode size (mean ± s.d.), determined by NTA, of the indicated EVs isolated from *Anxa6*-WT (top) or *Anxa6*-KO (clone no. 1; bottom) 4T1-mCh cells. The data show results from $n = 5$ (*Anxa6*-WT) and $n = 3$ (*Anxa6*-KO) independent EV preparations. **g**, Concentration (mean ± s.e.m.; $n = 3$ acquisitions of one sample per condition) and size distribution of EVs isolated from medium conditioned by CREMO- or PTX-treated *Anxa6*-KO 4T1-mCh cells (clone no. 1), determined by NTA. **h**, 4T1-mCh$^+$ metastatic area fraction per lung section (mean ± s.e.m.) in *Rag1*$^{-/-}$ mice pre-conditioned with *Anxa6*-WT or *Anxa6*-KO (clone no. 1) EVs. $n = 7$ mice for all test groups. The statistical analyses were performed using two-way ANOVA with Tukey's multiple comparison tests. Representative images of lung sections stained with DAPI are shown on the right; the mCh signal was acquired as direct fluorescence. Scale bars, 1 mm. **i**, 4T1-mCh$^+$ metastatic area fraction per lung section (mean ± s.e.m.) in *Rag1*$^{-/-}$ mice pre-conditioned with *Anxa6*-WT or *Anxa6*-KO (clone no. 1) EVs. $n = 8$ mice for all groups except $n = 7$ mice for the DMSO-EV/*Anxa6*-WT group. Statistical analysis was performed as in **h**. The source data are shown in Supplementary Table 5. Unprocessed blots are shown in Supplementary Fig. 9.

tumour metastasis. To test this possibility, we generated *Anxa6* knockout (KO) 4T1-mCh cells using clustered regularly interspaced short palindromic repeats (CRISPR)–CRISPR associated protein 9 (Cas9) technology (Fig. 4a). We obtained two *Anxa6*-deficient clones (Fig. 4b) that were used in subsequent experiments. ANXA6 was exhaustively depleted from *Anxa6*-KO 4T1-mCh-derived

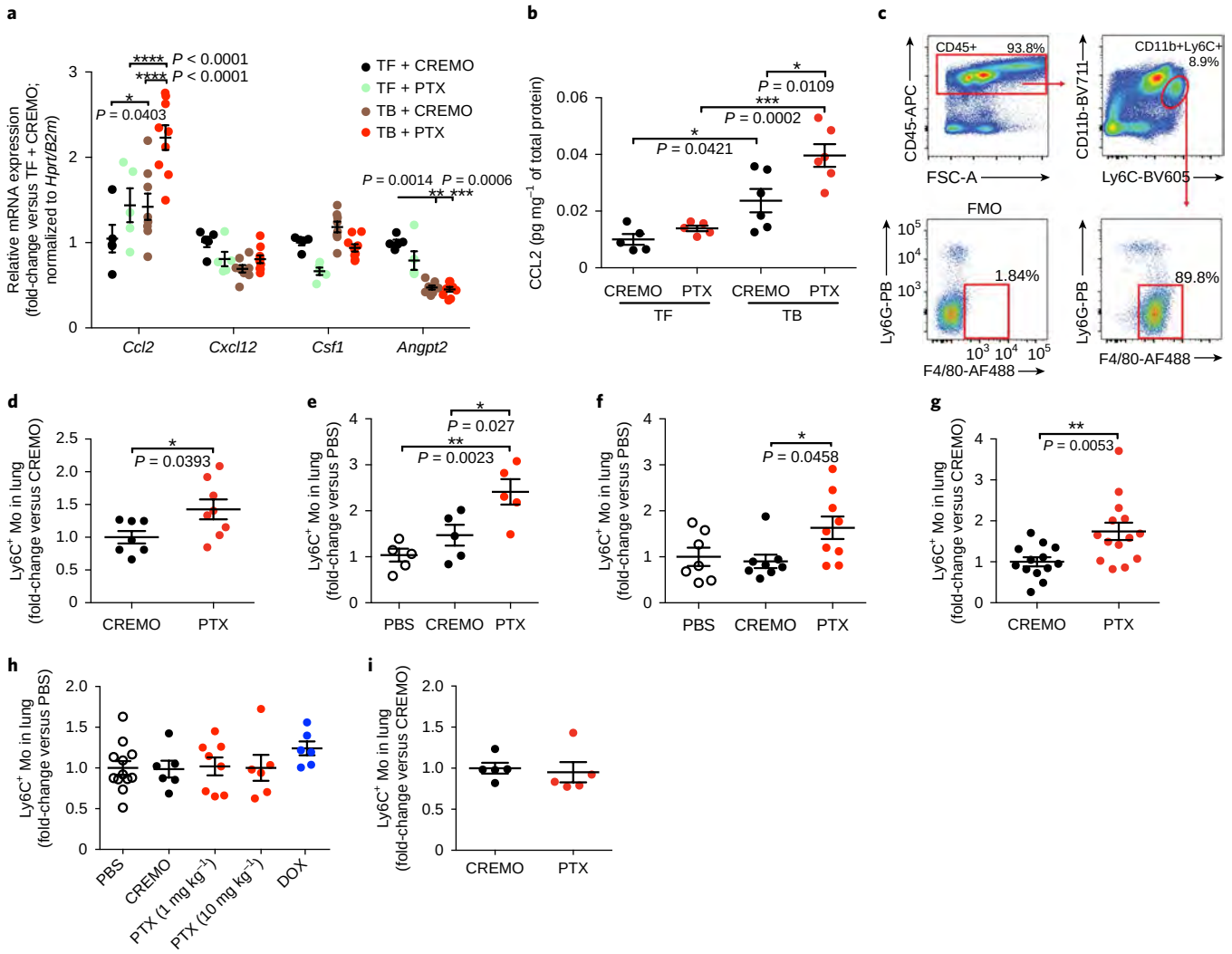

Fig. 5 | PTX induces CCL2 expression and Ly6C⁺ monocyte expansion in the lungs of mammary tumour-bearing mice. a, qPCR analysis of the indicated genes (mean ± s.e.m.) in the lungs of tumour-free (TF) and 4T1 tumour-bearing (TB) mice treated as indicated. TF + CREMO, $n = 5$; TF + PTX, $n = 5$; TB + CREMO, $n = 8$ and TB + PTX, $n = 9$ mice. The statistical analyses were performed by two-way ANOVA with Tukey's multiple comparison tests. **b**, ELISA-based CCL2 protein (mean ± s.e.m.) in the lungs of mice treated as in **a**. $n = 5$ and 6 mice each for the TF and TB groups, respectively. The statistical analyses were performed as in **a**. **c**, FACS analysis of CD45⁺CD11b⁺Ly6C⁺Ly6G⁻F4/80⁺ monocytes (Ly6C⁺ Mo) in the lungs of tumour-bearing mice. A representative sample is shown to illustrate the gating strategy. FMO, fluorescence minus one. **d**–**g**, FACS analysis of Ly6C⁺ Mo (mean ± s.e.m.) in tumour-bearing mice treated as indicated. The data show the frequency of Ly6C⁺ monocytes in the CD45⁺ population relative to control (CREMO or PBS). **d**, 4T1-mCh tumours in *Rag1*$^{-/-}$mice; $n = 7$ and 8 mice for the CREMO and PTX groups, respectively. **e**, 4T1 tumours in Balb/c mice; $n = 5$ mice for all groups. **f**, 4T1-mCh/HER2 tumours in Swiss nu/nu mice; $n = 7$, 8 and 9 mice for the PBS, CREMO and PTX groups, respectively. **g**, MMTV-PyMT mice, $n = 13$ and 14 mice for the CREMO and PTX groups, respectively. The statistical analyses were performed using unpaired two-tailed Student's *t*-tests (**d**,**g**) or one-way ANOVA with Tukey's multiple comparison tests (**e**,**f**). The data in **g** show three independent experiments combined. **h**,**i**, FACS analysis of Ly6C⁺ Mo (mean ± s.e.m.) in the lungs of tumour-free FVB/*n* (**h**) or *Rag1*$^{-/-}$ (**i**) mice treated as indicated and analysed two days after treatment. **h**, $n = 12$, 6, 8, 6 and 6 mice for the PBS, CREMO, PTX 1 mg kg^{-1}, PTX 10 mg kg^{-1} and DOX groups, respectively. **i**, $n = 5$ mice for both groups. The statistical analyses were performed using one-way ANOVA with Tukey's multiple comparison tests (**h**) or unpaired two-tailed Student's *t*-tests (**i**). The source data are shown in Supplementary Table 5.

EVs treated with either CREMO or PTX (Fig. 4c). ANXA6 deficiency in 4T1-mCh cells did not impair the enhancement of EV release by PTX (Fig. 4d); furthermore, *Anxa6*-proficient (WT) and KO EVs could not be distinguished by TEM (Fig. 4e) and NTA (Fig. 4f,g) analysis.

We then isolated *Anxa6*-WT and KO EVs from 4T1-mCh cells treated in vitro with either PTX or DOX (or the appropriate vehicle) to pre-condition *Rag1*$^{-/-}$ mice before the intravenous injection of 4T1-mCh cells, according to a lung colonization assay (Fig. 2b). Remarkably, ANXA6 deficiency in PTX-EV or DOX-EV disrupted their capacity to facilitate lung colonization by 4T1-mCh cells (Fig. 4h,i). The depletion of ANXA6 from 4T1 cells (Supplementary Fig. 4i) did not alter the loading of PTX or DOX into EVs (Supplementary Fig. 4j), arguing against the possibility that ANXA6-deficient EVs had compromised pro-metastatic capacity owing to changes in intravesicular drug levels, which were negligible irrespective of ANXA6 status (Supplementary Fig. 4k).

PTX induces CCL2 expression and Ly6C⁺ monocyte expansion in lungs of mammary tumour-bearing mice. We analysed

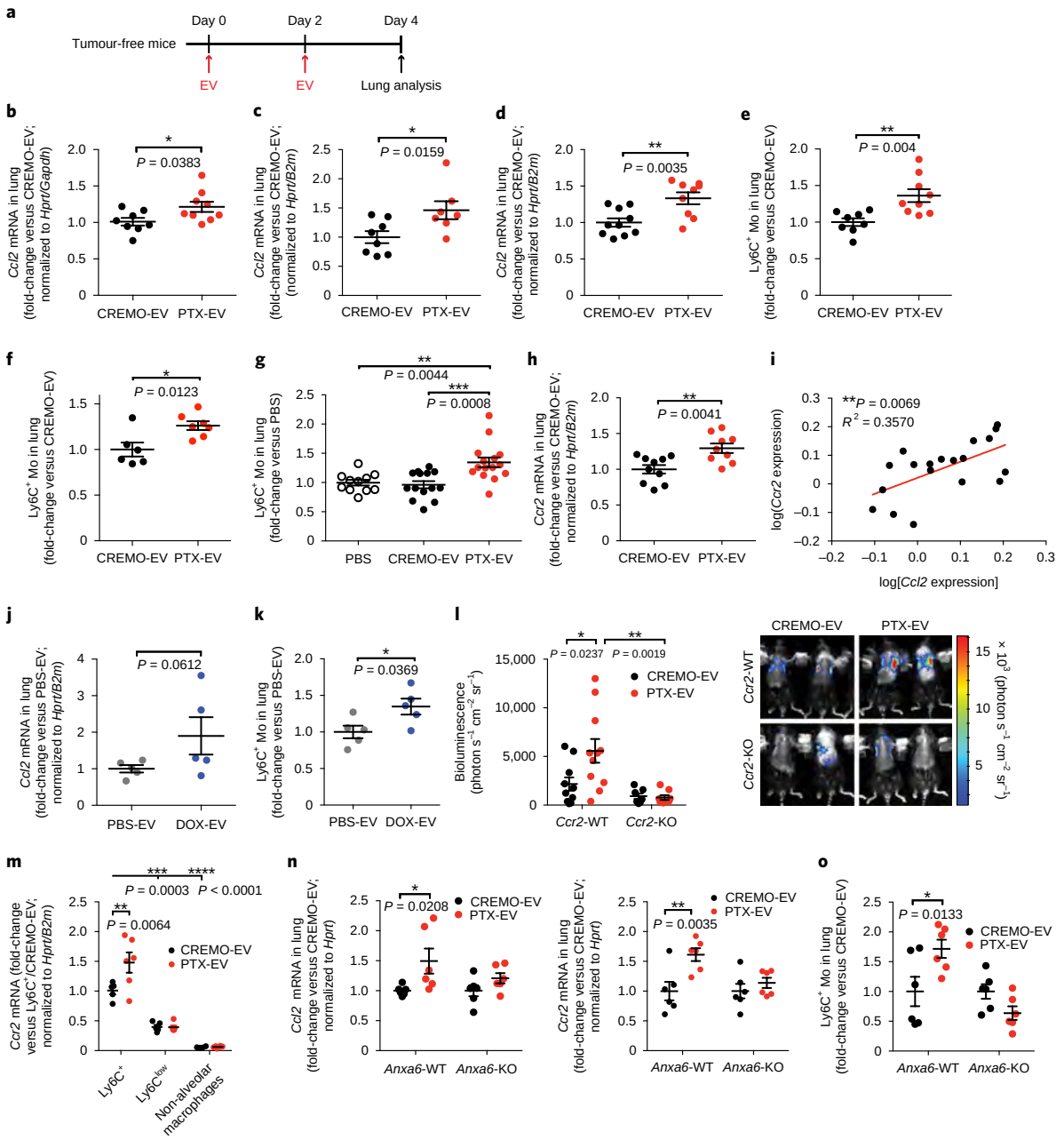

Fig. 6 | Ly6C+ monocytes mediate the pro-metastatic activity of chemotherapy-elicited EVs. a,Schematic of EV pre-conditioning studies in tumour-free mice. **b**–**d**, qPCR analysis of *Ccl2* expression (mean ± s.e.m.) in the lungs of tumour-free mice that received EVs. **b**, 4T1 EVs in Balb/c mice; CREMO-EV, $n = 8$; PTX-EV, $n = 9$. **c**, 4T1-mCh EVs in *Rag1*$^{-/-}$mice; CREMO-EV, $n = 8$; PTX-EV, $n = 7$. **d**, MMTV-PyMT tumour-derived EVs in FVB/n mice; CREMO-EV, $n = 10$; PTX-EV, $n = 9$. The statistical analyses were performed using unpaired two-tailed Student's *t*-tests. **e**–**g**, FACS analysis of Ly6C+ Mo (mean ± s.e.m.) in the lungs of tumour-free mice that received EVs. **e**, 4T1 EVs in Balb/c mice; CREMO-EV, $n = 8$; PTX-EV, $n = 9$. **f**, 4T1-mCh EVs in *Rag1*$^{-/-}$ mice; CREMO-EV, $n = 6$; PTX-EV, $n = 7$. **g**, MMTV-PyMT tumour-derived EVs in FVB/n mice; PBS (no EVs), $n = 11$; CREMO-EV, $n = 14$; PTX-EV, $n = 15$. The statistical analyses were performed using unpaired two-tailed Student's *t*-tests (**e**,**f**) or one-way ANOVA with Tukey's multiple comparison tests (**g**). **h**, qPCR analysis of *Ccr2* expression (mean ± s.e.m.) in the lungs of FVB/n mice that received MMTV-PyMT tumour-derived CREMO-EV ($n = 10$) or PTX-EV ($n = 9$). Statistical analysis performed as in **b**. **i**, Correlation between *Ccl2* and *Ccr2* transcript levels in the lungs of FVB/n mice shown in **d** and **h**. The Pearson correlation coefficient (R^2) is indicated. **j**,**k**, qPCR analysis of *Ccl2* expression (**j**) and FACS analysis of Ly6C+ Mo (**k**) in the lungs of tumour-free FVB/n mice (mean ± s.e.m.) that received MMTV-PyMT tumour-derived PBS-EV ($n = 5$) or DOX-EV ($n = 5$). Statistical analysis performed as in **b**. **l**, Bioluminescence analysis (total photon flux; mean ± s.e.m.) of *Ccr2* WT or KO mice pre-conditioned with the indicated EVs and analysed 10 days after the injection of E0771-LG:FI cells. The right panel shows images of representative mice. CREMO-EV/*Ccr2*-WT, $n = 10$; PTX-EV/*Ccr2*-WT, $n = 11$; CREMO-EV/*Ccr2*-KO, $n = 7$; PTX-EV/*Ccr2*-KO, $n = 8$. The statistical analyses were performed using two-way ANOVA with Tukey's multiple comparison tests. The data show three independent experiments combined. **m**, qPCR analysis of *Ccr2* expression (mean ± s.e.m.) in myeloid cells (Ly6C+ Mo; Ly6C^{low} Mo and non-alveolar macrophages) FACS-sorted from the lungs of tumour-free mice that received MMTV-PyMT tumour-derived CREMO-EV ($n = 5$, except non-alveolar macrophages where $n = 4$) or PTX-EV ($n = 6$). Statistical analysis as in **l**. **n**,**o**, qPCR analysis of *Ccl2* and *Ccr2* expression (**n**) and FACS analysis of Ly6C+ Mo (**o**) in the lungs of *Rag1*$^{-/-}$ mice (mean ± s.e.m; $n = 6$ mice per group) that received CREMO-EV or PTX-EV from either *Anxa6*-WT or *Anxa6*-KO 4T1-mCh cells. The statistical analyses were performed using two-way ANOVA with Sidak's multiple comparison tests. The source data are shown in Supplementary Table 5.

the expression of cytokines known to facilitate mammary tumour metastasis, such as C–C motif chemokine ligand 2 (CCL2), C–X–C motif chemokine 12 (CXCL12), colony-stimulating factor 1 (CSF1) and angiopoietin 2 (ANGPT2)[45], in the lungs of tumour-free and 4T1-mCh tumour-bearing *Rag1*$^{-/-}$ mice that were treated with either PTX or CREMO. Treatment with PTX significantly increased *Ccl2* expression at both the mRNA (Fig. 5a) and protein (Fig. 5b) level in the lungs of 4T1-mCh tumour-bearing but not tumour-free mice.

CCL2 was previously reported to enhance Ly6C$^+$CCR2$^+$ monocyte-assisted metastasis of mammary tumours[46–49]. Consistent with the upregulation of CCL2, PTX increased the relative abundance of Ly6C$^+$ monocytes in the lungs of 4T1-mCh tumour-bearing *Rag1*$^{-/-}$ mice, 4T1 tumour-bearing Balb/c mice, 4T1-mCh/HER2 tumour-bearing Swiss nu/nu mice and transgenic MMTV-PyMT mice compared with the vehicle (Fig. 5c–g). Conversely, PTX did not alter the relative abundance of Ly6C$^+$ monocytes in the lungs of tumour-free mice (Fig. 5h,i). These results indicate that signals emanating from primary tumours are required for PTX-induced upregulation of CCL2 and expansion of Ly6C$^+$ monocytes in the lungs.

Chemotherapy-elicited EVs induce pulmonary CCL2 expression and Ly6C$^+$ monocyte expansion. We examined whether the effects of PTX on CCL2 and Ly6C$^+$ monocytes were dependent on EVs. To this aim, we performed pre-conditioning studies with EVs in tumour-free mice (Fig. 6a). PTX-EVs isolated from 4T1 or 4T1-mCh cells increased *Ccl2* expression in the lungs of Balb/c and *Rag1*$^{-/-}$ tumour-free mice, respectively (Fig. 6b,c). We obtained similar results when we pre-conditioned tumour-free FVB/n mice with PTX-EV isolated ex vivo from MMTV-PyMT tumour-derived cells (Figs. 2d and 6d). In parallel with *Ccl2* expression, the relative abundance of lung Ly6C$^+$CCR2$^+$ monocytes increased in response to PTX-EV (Fig. 6e–i). Notably, both the levels of *Ccl2* expression and Ly6C$^+$ monocytes were also elevated in response to DOX-EV isolated ex vivo from MMTV-PyMT tumour-derived cells (Fig. 6j,k).

The pro-metastatic capacity of chemotherapy-elicited EVs is dependent on Ly6C$^+$CCR2$^+$ monocytes and ANXA6. To explore the functional involvement of Ly6C$^+$CCR2$^+$ monocytes in PTX-EV-mediated pulmonary metastasis, we performed pre-conditioning experiments with EVs in *Ccr2* KO mice (C57Bl/6 background) that have impaired monocyte-assisted mammary cancer metastasis[49]. Whereas PTX-EV derived from E0771-LG mouse mammary carcinoma cells enhanced pulmonary seeding of firefly luciferase-expressing E0771-LG:Fl cells in *Ccr2* WT mice, they failed to do so in *Ccr2* KO mice (Fig. 6l). Interestingly, *Ccr2* expression was upregulated in Ly6C$^+$ monocytes, but not other myeloid cells, that were sorted from the lungs of tumour-free FVB/n mice pre-conditioned with PTX-EV (Fig. 6m). These data strongly argue that Ly6C$^+$CCR2$^+$ monocytes mediate EV-induced, pulmonary mammary cancer metastasis.

Because *Anxa6* KO PTX-EV failed to enhance pulmonary colonization by 4T1-mCh cells (Fig. 4h,i), we investigated whether the PTX-EV-mediated effects on pulmonary CCL2 expression and Ly6C$^+$ monocyte expansion were also dependent on ANXA6 in EVs. The deficiency of ANXA6 in PTX-EV isolated from 4T1-mCh cells prevented *Ccl2* and *Ccr2* upregulation (Fig. 6n) and the increase of Ly6C$^+$ monocytes (Fig. 6o) in the lungs of *Rag1*$^{-/-}$ mice. Together, these results indicate that chemotherapy-induced enrichment of ANXA6 in mammary tumour-derived EVs supports a pro-metastatic cascade in the lung that is dependent on local Ly6C$^+$ monocyte expansion.

Chemotherapy-elicited EVs promote inflammatory EC activation through ANXA6 transfer. The internalization of breast cancer-derived EVs into lung endothelial cells (ECs) may influence the initial steps of pulmonary metastasis by altering the biology of those cells in the pre-metastatic niche[24,50]. We observed increased proportions of lung ECs displaying mCh fluorescence after 4T1-mCh tumour-bearing *Rag1*$^{-/-}$ or 4T1-mCh/HER2 tumour-bearing Swiss nu/nu mice were treated with PTX, compared with mice treated with CREMO (Fig. 7a–c).

Increased mCh fluorescence in lung ECs may denote internalization of tumour-derived EVs, a process that can occur through EV–cell fusion[51]. We next used the murine EC line bEnd.3 to study the effects of EVs on ECs. The bEnd.3 cells internalized mCh$^+$ EVs in a dose-dependent manner (Supplementary Fig. 5a,b); interestingly, bEnd.3 cells that were exposed to medium conditioned by PTX-treated 4T1-mCh or PyMT-IK1-mCh cancer cells displayed higher mCh fluorescence than bEnd.3 cells that were exposed to medium conditioned by CREMO-treated cells (Supplementary Fig. 5c). Moreover, PTX-EVs from either 4T1-mCh or PyMT-IK1-mCh cells were internalized by bEnd.3 cells more efficiently than matched amounts of CREMO-EVs (Supplementary Fig. 5d). Finally, the uptake of EVs by bEnd.3 cells was independent of ANXA6 (Supplementary Fig. 5e), which suggests that other molecules (Supplementary Table 1), such as integrins[38], could mediate the preferential uptake of PTX-EV.

PTX-EVs that were isolated from either 4T1-mCh or PyMT-IK1-mCh cells transferred ANXA6 (and mCh) to bEnd.3 cells that were made *Anxa6*-deficient using CRISPR–Cas9 (Fig. 7d and Supplementary Fig. 6a,b). A Duolink proximity ligation assay, which enables the imaging of protein pairs that co-localize within 40 nm, indicated that PTX-EV-mediated transfer of ANXA6 to *Anxa6* KO bEnd.3 cells was conducive to ANXA6 co-localization with the nuclear factor kappa-light-chain-enhancer of activated B cells (NF-kB) subunit p65 (Fig. 7e and Supplementary Fig. 6c,d), which is consistent with the ability of ANXA6 to interact with p65 (ref. [52]). Notably, matched doses of CREMO-EV did not reveal detectable ANXA6/p65 proximity in the same assay, possibly because PTX-EV fuse more efficiently than CREMO-EV with bEnd.3 cells (Supplementary Fig. 5c–e) and contain higher quantities of ANXA6 than CREMO-EV (Fig. 3d–j).

NF-kB (p65/*Rela*) activates *Ccl2* transcription[53]. To gain insight into a potential mechanistic link between ANXA6 transfer to ECs and *Ccl2* upregulation, we generated *Rela* (p65) KO bEnd.3 cells that had defective NF-kB activation and *Ccl2* expression (Fig. 7f and Supplementary Fig. 6e). PTX-EVs isolated from 4T1-mCh cells failed to induce NF-kB activation (Fig. 7g) and *Ccl2* upregulation (Fig. 7h) in *Rela* KO bEnd.3 cells. Conversely, PTX-EVs isolated from 4T1-mCh or PyMT-IK1 cells increased NF-kB activity and *Ccl2* expression in *Rela*-proficient bEnd.3 cells; notably, these responses required ANXA6 in EVs. Accordingly, *Anxa6* KO bEnd.3 cells had defective NF-kB activation and *Ccl2* transcription in response to tumour-necrosis factor (TNF) compared with *Anxa6* WT cells; notably, neither *Csf1* nor *Cxcl12* were regulated by ANXA6 (Supplementary Fig. 6f–i). Similar to PTX-EV, DOX-EVs from 4T1 cells increased the levels of *Ccl2* transcripts (Fig. 7i) and NF-kB activity (Fig. 7j) in bEnd.3 cells. Therefore, EV-associated ANXA6 triggers an NF-kB-dependent pro-inflammatory response in ECs.

We then examined whether PTX-EV could activate *Ccl2* transcription in lung ECs, which are a source of CCL2 in mammary tumour-bearing mice[54]. We used fluorescence-activated cell sorting (FACS) to isolate lung ECs of tumour-free FVB/n mice that were pre-conditioned with MMTV-PyMT tumour-derived PTX-EVs or CREMO-EVs (Fig. 2d) and found enhanced *Ccl2* expression in lung ECs exposed to PTX-EVs (Fig. 7k). Together, these findings suggest that chemotherapy-elicited tumour EVs promote pro-inflammatory EC activation, CCL2 upregulation, Ly6C$^+$ monocyte accumulation and tumour colonization at metastatic sites through a mechanism

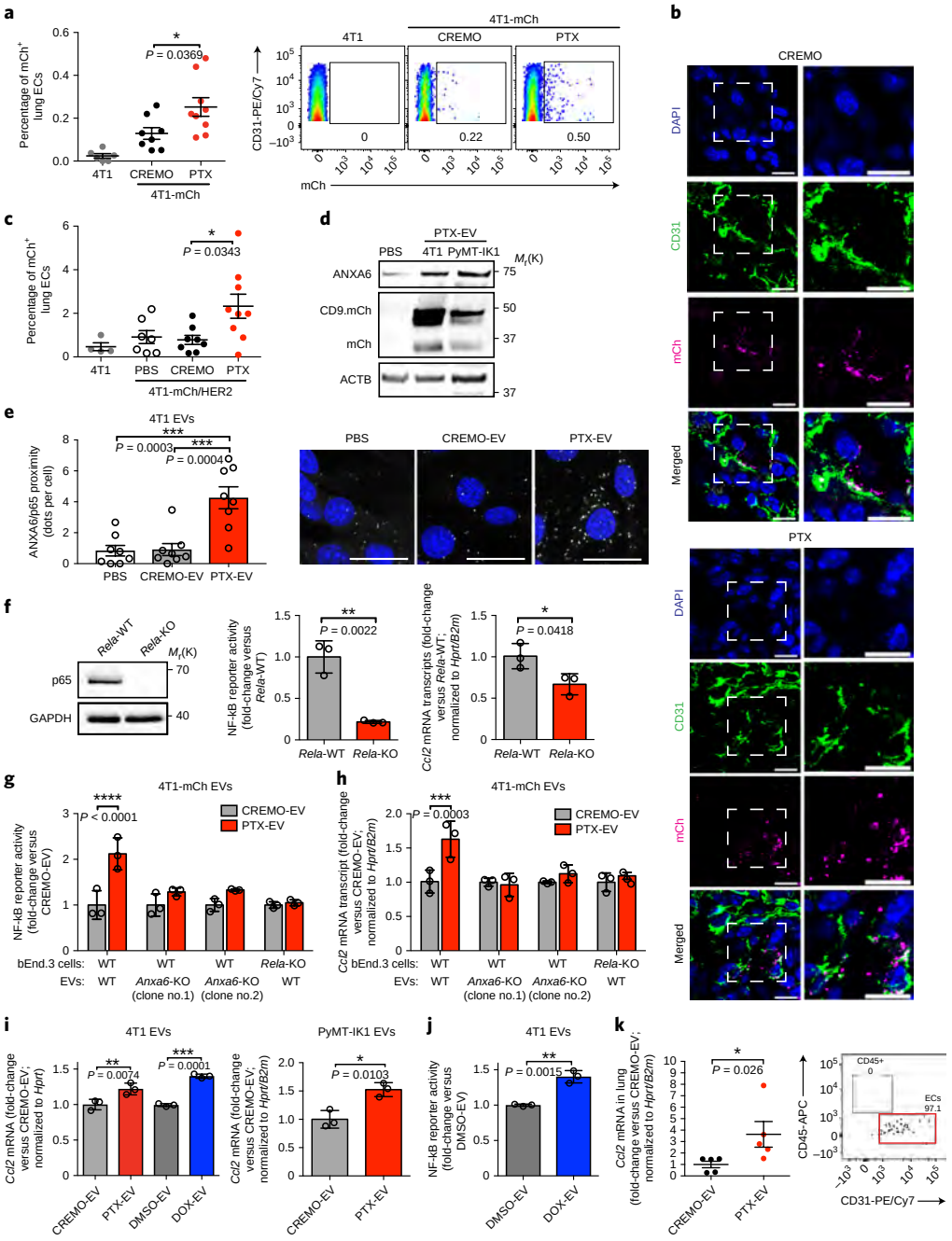

Fig. 7 | Chemotherapy-elicited EVs promote inflammatory EC activation through ANXA6 transfer. a, FACS of mCh⁺ ECs (mean ± s.e.m.) in the lungs of 4T1 ($n = 6$) and 4T1-mCh (CREMO, $n = 8$; PTX, $n = 9$) tumour-bearing *Rag1*$^{-/-}$ mice. Statistical analysis performed using one-way ANOVA with Tukey's multiple comparison test. The right panels show the gating strategy employed. **b**, Representative confocal images of anti-CD31 endothelial and anti-mCh immunostaining of lung sections from 4T1-mCh tumour-bearing *Rag1*$^{-/-}$ mice treated as in **a**; nuclei are stained with DAPI. Scale bars, 10 µm. **c**, FACS of mCh⁺ ECs (mean ± s.e.m.) from the lungs of 4T1 ($n = 4$) and 4T1-mCh/HER2 (PBS, $n = 7$; CREMO, $n = 8$; PTX, $n = 9$) tumour-bearing Swiss nu/nu mice. Statistical analysis performed as in **a**. **d**. Western blot analysis of the indicated proteins in *Anxa6*-KO bEnd.3 cells treated with PBS or the indicated EVs. The experiment was performed twice; Supplementary Fig. 6b shows a replicate experiment. **e**, Duolink staining of *Anxa6*-KO bEnd.3 cells showing ANXA6/p65 proximity (number of white dots per cell; mean ± s.e.m.; $n = 8$ randomly selected images, each containing at least 12 cells). The statistical analyses were performed as in **a**. The right panels show representative images; nuclei are stained with DAPI (blue). Scale bars, 30 µm. The data show one experiment of the two performed. **f**, Western blot analysis of p65 (left), NF-kB activity (middle) and qPCR of *Ccl2* expression (right) in bEnd.3 cells (mean ± s.d.; $n = 3$ independent cell cultures per condition). Statistical analysis was performed using an unpaired two-tailed Student's *t*-test. **g**,**h**. NF-kB activity (**g**) and qPCR of *Ccl2* expression (**h**) in bEnd.3 cells (mean ± s.d.; $n = 3$ independent cell cultures/condition). Statistical analyses were performed using two-way ANOVA with Sidak's multiple comparison tests. The data show one experiment of two (**g**) or three (**h**) performed. **i**,**j**. qPCR analysis of *Ccl2* expression (**i**) and NF-kB activity (**j**) in bEnd.3 cells (mean ± s.d.; $n = 3$ independent cell cultures per condition). Statistical analyses were performed using two-way ANOVA with Tukey's multiple comparison tests (**i**, left) or unpaired two-tailed Student's *t*-tests (**i**, right panel and **j**). **k**, qPCR of *Ccl2* expression in mCh⁺CD31⁺CD45⁻ ECs sorted from the lungs of FVB/n mice (mean ± s.e.m.; $n = 5$ mice). Statistical analysis was performed using unpaired one-tailed Student's *t*-test. The right panel shows the purity of the sorted ECs. The source data are shown in Supplementary Table 5. Unprocessed blots are shown in Supplementary Fig. 9.

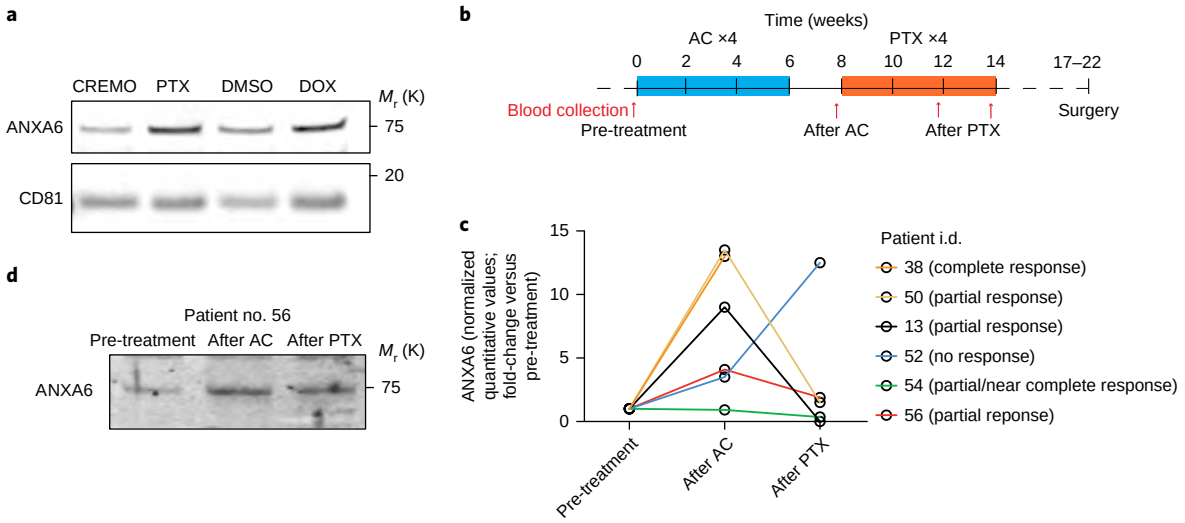

Fig. 8 | ANXA6 is detected in circulating EVs of breast cancer patients undergoing neoadjuvant chemotherapy. a, Western blot analysis of ANXA6 and CD81 in EVs isolated from MDA-MB-231 cells treated as indicated. The experiment was performed three times for PTX and once for DOX treatment. **b**, Schematic of the treatment timeline and time-points of blood collection in breast cancer patients ($n=6$). AC, anthracycline (DOX) plus cyclophosphamide. **c**, LC–MS/MS-based quantification of ANXA6 in EVs isolated from the plasma of breast cancer patients ($n=6$) before chemotherapy (pre-treatment), after AC and after PTX treatment. The data show the quantitative values of ANXA6 presented as fold-change versus the pre-treatment level. Note that the amount of EVs that could be isolated from patient no. 38 after treatment with PTX was insufficient to perform LC–MS/MS analysis. The tumour response was assessed at the time of surgery. **d**, Western blot analysis of ANXA6 in the plasma EVs of patient no. 56 analysed at the indicated time-points. The experiment was performed once. The source data are shown in Supplementary Table 5. Unprocessed blots are shown in Supplementary Fig. 9.

that involves the horizontal transfer of EV-associated ANXA6 to the pulmonary endothelium.

Chemotherapy-elicited EVs display broad cellular tropism in tumour-bearing mice. Besides ECs, other lung-resident cells may mediate metastasis in response to chemotherapy-induced EVs. CD11b$^+$Gr1$^-$ lung macrophages/monocytes also internalized mCh$^+$ EVs in PTX-treated, 4T1-mCh *Rag1*$^{-/-}$ or 4T1-mCh/HER2 Swiss nu/nu tumour-bearing mice (Supplementary Fig. 7a,b). Moreover, PTX-EVs isolated from MMTV-PyMT tumour-derived cells upregulated interleukin-6 (*Il6*) expression in the lung (Supplementary Fig. 7c) and, specifically, lung-associated non-alveolar macrophages (Supplementary Fig. 7d) of tumour-free FVB/n mice; notably, IL-6 was previously implicated in chemotherapy resistance[55] and macrophage-assisted mammary tumour metastasis[47,56].

Finally, PTX-EV transferred mCh to liver sinusoidal ECs more efficiently than CREMO-EVs (Supplementary Fig. 7e,f), which suggests that chemotherapy-elicited EVs might also promote breast cancer metastasis to the liver. However, the rapid growth kinetics of both primary tumours and pulmonary metastasis in the breast cancer models employed in our study complicate the assessment of slow-growing liver metastases.

ANXA6 is detected in circulating EVs of breast cancer patients undergoing neoadjuvant chemotherapy. We finally investigated the effects of chemotherapy on EV-associated ANXA6 in human breast cancer cells and patients with breast cancer. Both PTX and DOX increased ANXA6 protein levels in EVs released by human MDA-MB-231 breast cancer cells (Fig. 8a). Furthermore, EVs purified from the plasma of breast cancer patients undergoing neoadjuvant chemotherapy (Supplementary Table 2 and Fig. 8b) had increased ANXA6 content, quantified by LC–MS/MS, in five out of six cases, compared with pre-treatment levels (Fig. 8c, Supplementary Fig. 8 and Supplementary Table 3). Because the amounts of EVs we could isolate from each sample were limited, we were only able to verify the LC–MS/MS data by western blotting in one case (patient no. 56; Fig. 8d). Notably, ANXA6 levels in the EVs decreased at the end of neoadjuvant therapy in the patients who achieved a partial or complete response (five out of six), probably reflecting shrinkage of the tumour in response to chemotherapy. In addition, the finding that EV-associated ANXA6 levels increased on-therapy in one patient with progressive disease (patient no. 52) strongly suggests that EV-associated ANXA6 was in fact of cancer cell origin. Although limited, these data support the notion that chemotherapy augments ANXA6 levels in the circulating EVs of patients with breast cancer.

Discussion

Neoadjuvant chemotherapy improves the management of invasive breast cancer by inducing pathological complete responses that are associated with a significantly reduced risk of recurrence in a fraction of the patients[1–6]. However, therapy-induced host responses[7], such as those described in our study, may limit the benefits of pre-operative treatments in some patients. It is tempting to speculate that human primary breast tumours that fail to readily regress on neoadjuvant chemotherapy (a condition of partial or complete chemoresistance) may also release pro-metastatic EVs that in turn facilitate the seeding, survival or early colonization of metastatic niches by chemoresistant cancer cells. However, it should be cautioned that we did not study the survival of mice in association with the various treatments, so we currently ignore whether increased metastatic seeding and outgrowth in response to chemotherapy-elicited EVs would translate into shorter survival in our experimental cancer models.

The potential participation of tumour-derived EVs in the process of human breast cancer metastasis is poorly understood at present and may be challenging to explore given the lack of validated breast-cancer-specific EV markers[57]. In the future, chemotherapy-elicited EVs might provide biomarkers for predicting metastasis risk associated with neoadjuvant chemotherapy in patients who do not achieve a complete response. Interestingly, ANXA6 has been

detected in EVs isolated from the MDA-MB-231-derived clone 4175 that exhibits lung tropism[20]. Furthermore, EV-associated ANXA6 has been implicated in the progression of pancreatic cancer in a mouse model[42]. The significance of EV-associated ANXA6 for breast cancer metastasis may, therefore, merit further investigation.

Online content

Any methods, additional references, Nature Research reporting summaries, source data, statements of data availability and associated accession codes are available at https://doi.org/10.1038/s41556-018-0256-3.

Received: 4 September 2016; Accepted: 20 November 2018;
Published online: 31 December 2018

References

1. Rastogi, P. et al. Preoperative chemotherapy: updates of National Surgical Adjuvant Breast and Bowel Project Protocols B-18 and B-27. *J. Clin. Oncol.* **26**, 778–785 (2008).
2. Fisher, E. R. et al. Pathobiology of preoperative chemotherapy: fi dings from the National Surgical Adjuvant Breast and Bowel (NSABP) protocol B-18. *Cancer* **95**, 681–695 (2002).
3. DeMichele, A., Yee, D. & Esserman, L. Mechanisms of resistance to neoadjuvant chemotherapy in breast cancer. *N. Engl. J. Med.* **377**, 2287–2289 (2017).
4. Spring, L. et al. Pathologic complete response after neoadjuvant chemotherapy and long-term outcomes among young women with breast cancer. *J. Natl Compr. Canc. Netw.* **15**, 1216–1223 (2017).
5. Zardavas, D. & Piccart, M. Neoadjuvant therapy for breast cancer. *Annu. Rev. Med.* **66**, 31–48 (2015).
6. Gampenrieder, S. P., Rinnerthaler, G. & Greil, R. Neoadjuvant chemotherapy and targeted therapy in breast cancer: past, present, and future. *J. Oncol.* **2013**, 732047 (2013).
7. Shaked, Y. Balancing efficacy of and host immune responses to cancer therapy: the yin and yang effects. *Nat. Rev. Clin. Oncol.* **13**, 611–626 (2016).
8. Karagiannis, G. S. et al. Neoadjuvant chemotherapy induces breast cancer metastasis through a TMEM-mediated mechanism. *Sci. Transl. Med.* **9**, eaan0026 (2017).
9. Voloshin, T. et al. Blocking IL1β pathway following paclitaxel chemotherapy slightly inhibits primary tumor growth but promotes spontaneous metastasis. *Mol. Cancer Ther.* **14**, 1385–1394 (2015).
10. Volk-Draper, L. et al. Paclitaxel therapy promotes breast cancer metastasis in a TLR4-dependent manner. *Cancer Res.* **74**, 5421–5434 (2014).
11. Liu, G. et al. Specific chemotherapeutic agents induce metastatic behaviour through stromal- and tumour-derived cytokine and angiogenic factor signalling. *J. Pathol.* **237**, 190–202 (2015).
12. Chang, Y. S., Jalgaonkar, S. P., Middleton, J. D. & Hai, T. Stress-inducible gene *Atf3* in the noncancer host cells contributes to chemotherapy-exacerbated breast cancer metastasis. *Proc. Natl Acad. Sci. USA* **114**, E7159–E7168 (2017).
13. Daenen, L. G. et al. Chemotherapy enhances metastasis formation via VEGFR-1-expressing endothelial cells. *Cancer Res.* **71**, 6976–6985 (2011).
14. De Palma, M., Biziato, D. & Petrova, T. V. Microenvironmental regulation of tumour angiogenesis. *Nat. Rev. Cancer* **17**, 457–474 (2017).
15. De Palma, M. et al. Tie2 identifies a hematopoietic lineage of proangiogenic monocytes required for tumor vessel formation and a mesenchymal population of pericyte progenitors. *Cancer Cell.* **8**, 211–226 (2005).
16. Harney, A. S. et al. Real-time imaging reveals local, transient vascular permeability, and tumor cell intravasation stimulated by TIE2hi macrophage-derived VEGFA. *Cancer Discov.* **5**, 932–943 (2015).
17. Costa-Silva, B. et al. Pancreatic cancer exosomes initiate pre-metastatic niche formation in the liver. *Nat. Cell Biol.* **17**, 816–826 (2015).
18. Becker, A. et al. Extracellular vesicles in cancer: cell-to-cell mediators of metastasis. *Cancer Cell.* **30**, 836–848 (2016).
19. Tkach, M. & Thery, C. Communication by extracellular vesicles: where we are and where we need to go. *Cell* **164**, 1226–1232 (2016).
20. Hoshino, A. et al. Tumour exosome integrins determine organotropic metastasis. *Nature* **527**, 329–335 (2015).
21. Yokoi, A. et al. Malignant extracellular vesicles carrying MMP1 mRNA facilitate peritoneal dissemination in ovarian cancer. *Nat. Commun.* **8**, 14470 (2017).
22. Zhou, W. et al. Cancer-secreted miR-105 destroys vascular endothelial barriers to promote metastasis. *Cancer Cell.* **25**, 501–515 (2014).
23. Kalluri, R. The biology and function of exosomes in cancer. *J. Clin. Invest.* **126**, 1208–1215 (2016).
24. Peinado, H. et al. Pre-metastatic niches: organ-specific homes for metastases. *Nat. Rev. Cancer* **17**, 302–317 (2017).
25. Guy, C. T., Cardiff, R. D. & Muller, W. J. Induction of mammary tumors by expression of polyomavirus middle T oncogene: a transgenic mouse model for metastatic disease. *Mol. Cell. Biol.* **12**, 954–961 (1992).
26. Lin, E. Y. et al. Progression to malignancy in the polyoma middle T oncoprotein mouse breast cancer model provides a reliable model for human diseases. *Am. J. Pathol.* **163**, 2113–2126 (2003).
27. DeNardo, D. G. et al. Leukocyte complexity predicts breast cancer survival and functionally regulates response to chemotherapy. *Cancer Discov.* **1**, 54–67 (2011).
28. Pulaski, B. A. & Ostrand-Rosenberg, S. Mouse 4T1 breast tumor model. *Curr. Protoc. Immunol.* **39**, 20.2.1–20.2.16 (2001).
29. Squadrito, M. L., Cianciaruso, C., Hansen, S. K. & De Palma, M. EVIR: chimeric receptors that enhance dendritic cell cross-dressing with tumor antigens. *Nat. Methods* **15**, 183–186 (2018).
30. Kowal, J. et al. Proteomic comparison defi es novel markers to characterize heterogeneous populations of extracellular vesicle subtypes. *Proc. Natl Acad. Sci. USA* **113**, E968–E977 (2016).
31. Thery, C., Amigorena, S., Raposo, G. & Clayton, A. Isolation and characterization of exosomes from cell culture supernatants and biological fluids. *Curr. Protoc. Cell Biol.* **30**, 3.22.1–3.22.29 (2006).
32. Montermini, L. et al. Inhibition of oncogenic epidermal growth factor receptor kinase triggers release of exosome-like extracellular vesicles and impacts their phosphoprotein and DNA content. *J. Biol. Chem.* **290**, 24534–24546 (2015).
33. Nakasone, E. S. et al. Imaging tumor-stroma interactions during chemotherapy reveals contributions of the microenvironment to resistance. *Cancer Cell* **21**, 488–503 (2012).
34. White, R., Rose, K. & Zon, L. Zebrafish cancer: the state of the art and the path forward. *Nat. Rev. Cancer* **13**, 624–636 (2013).
35. Teng, Y. et al. Evaluating human cancer cell metastasis in zebrafish. *BMC Cancer* **13**, 453 (2013).
36. Bobrie, A. et al. Rab27a supports exosome-dependent and -independent mechanisms that modify the tumor microenvironment and can promote tumor progression. *Cancer Res.* **72**, 4920–4930 (2012).
37. Ostrowski, M. et al. Rab27a and Rab27b control different steps of the exosome secretion pathway. *Nat. Cell Biol.* **12**, 19–30 (2010).
38. van Niel, G., D'Angelo, G. & Raposo, G. Shedding light on the cell biology of extracellular vesicles. *Nat. Rev. Mol. Cell Biol.* **19**, 213–228 (2018).
39. Gerke, V. & Moss, S. E. Annexins: from structure to function. *Physiol. Rev.* **82**, 331–371 (2002).
40. Qi, H. et al. Role of annexin A6 in cancer. *Oncol. Lett.* **10**, 1947–1952 (2015).
41. Sakwe, A. M., Koumangoye, R., Guillory, B. & Ochieng, J. Annexin A6 contributes to the invasiveness of breast carcinoma cells by influencing the organization and localization of functional focal adhesions. *Exp. Cell Res.* **317**, 823–837 (2011).
42. Leca, J. et al. Cancer-associated fibroblast-derived annexin A6+ extracellular vesicles support pancreatic cancer aggressiveness. *J. Clin. Invest.* **126**, 4140–4156 (2016).
43. Kidd, J. F. et al. Paclitaxel affects cytosolic calcium signals by opening the mitochondrial permeability transition pore. *J. Biol. Chem.* **277**, 6504–6510 (2002).
44. Octavia, Y. et al. Doxorubicin-induced cardiomyopathy: from molecular mechanisms to therapeutic strategies. *J. Mol. Cell. Cardiol.* **52**, 1213–1225 (2012).
45. Steeg, P. S. Targeting metastasis. *Nat. Rev. Cancer* **16**, 201–218 (2016).
46. Qian, B. Z. et al. CCL2 recruits inflammatory monocytes to facilitate breast-tumour metastasis. *Nature* **475**, 222–225 (2011).
47. Bonapace, L. et al. Cessation of CCL2 inhibition accelerates breast cancer metastasis by promoting angiogenesis. *Nature* **515**, 130–133 (2014).
48. Doak, G. R., Schwertfeger, K. L. & Wood, D. K. Distant relations: macrophage functions in the metastatic niche. *Trends Cancer* **4**, 445–459 (2018).
49. Kitamura, T. et al. CCL2-induced chemokine cascade promotes breast cancer metastasis by enhancing retention of metastasis-associated macrophages. *J. Exp. Med.* **212**, 1043–1059 (2015).
50. Hiratsuka, S. et al. Primary tumours modulate innate immune signalling to create pre-metastatic vascular hyperpermeability foci. *Nat. Commun* **4**, 1853 (2013).
51. Yanez-Mo, M. et al. Biological properties of extracellular vesicles and their physiological functions. *J. Extracell. Vesicles* **4**, 27066 (2015).
52. Campbell, K. A. et al. Annexin A6 interacts with p65 and stimulates NF-κB activity and catabolic events in articular chondrocytes. *Arthritis Rheum.* **65**, 3120-3129 (2013).
53. Ueda, A. et al. NF-kappa B and Sp1 regulate transcription of the human monocyte chemoattractant protein-1 gene. *J. Immunol.* **153**, 2052–2063 (1994).

54. Srivastava, K. et al. Postsurgical adjuvant tumor therapy by combining anti-angiopoietin-2 and metronomic chemotherapy limits metastatic growth. *Cancer Cell.* **26**, 880–895 (2014).
55. Incio, J. et al. Obesity promotes resistance to anti-VEGF therapy in breast cancer by up-regulating IL-6 and potentially FGF-2. *Sci. Transl. Med.* **10**, eaag0945 (2018).
56. Zhang, H. et al. Circulating tumor microparticles promote lung metastasis by reprogramming inflammatory and mechanical niches via a macrophage-dependent pathway. *Cancer Immunol. Res.* **6**, 1046–1056 (2018).
57. Schwich, E. & Rebmann, V. The inner and outer qualities of extracellular vesicles for translational purposes in breast cancer. *Front. Immunol.* **9**, 584 (2018).
69. Consortium, E.-T. et al. EV-TRACK: transparent reporting and centralizing knowledge in extracellular vesicle research. *Nat. Methods* **14**, 228–232 (2017).
70. Vizcaino, J. A. et al. 2016 update of the PRIDE database and its related tools. *Nucleic Acids Res.* **44**, 11033 (2016).

Acknowledgements

We thank C. Rmili-Wyser, A. Bellotti, B. Torchia, D. Laoui (M.D.P.'s laboratory) and M. Duquette (R.K.J.'s laboratory) for help with some experiments; T. Kitamura (University of Edinburgh) for advice on lung colonization assays and for providing E0771-LG and E0771-LG:Fl cells and H.G. Augustin (DKFZ) for critical comments on the manuscript. The EPFL core facilities of flow cytometry (FCCF), histology (HCF) and bioimaging/optics platform (BIOp) are acknowledged for skilled technical assistance; R. Hamelin and M. Moniatte of the proteomics facility (PCF, EPFL) for performing LC–MS/MS on EVs; T.J. Chico for providing access to zebrafish lines in the aquarium at the University Sheffield and R. Klemke for the kind gift of CFP-MDA-MB-435 cells. This work was primarily funded by grants from the Swiss Cancer League (grant no. KFS-3007-08-2012), Swiss National Science Foundation (grant no. SNF 31003A-165963) and European Research Council (grant no. ERC EVOLVE-72505) to M.D.P. L.M.S. was supported by NIH grant no. KL2 TR001100. C.E.L. acknowledges support from Cancer Research UK (grant no. C11712/A13028), Yorkshire Cancer Research (grant no. S382) and Breast Cancer Now (grant nos 2016MayPR746 and 2016NovPCC003). M.L.I.-A. was supported by NIH (NCI 1R01CA197943). L.M.C. acknowledges support from a DOD BCRP Era of Hope Scholar Expansion Award (grant no. W81XWH-08-PRMRP-IIRA), Susan B Komen Foundation (grant no. KG110560) and Breast Cancer Research Foundation. A.B. was supported by Susan B Komen Foundation (grant no. CCR15224703). R.K.J. acknowledges support from the Ludwig Center at Harvard, National Foundation for Cancer Research and NCI (grant no. R35CA197743). J.W.P. was supported by the Wellcome Trust (grant no. 101067/Z/13/Z) and MRC (grant no. MR/N022556/1).

Author contributions

I.K. designed and performed most of the experiments, analysed and interpreted data and wrote the manuscript. C.C. designed and performed experiments, analysed and interpreted data and wrote the manuscript. E.G. and J.W.P. designed, performed and analysed experiments in *Ccr2* KO mice. M.L.S. designed lentiviral vectors for gene KO, overexpression and reporter activity. A.C., C.B., A.G. and G.B.F. assisted with some experiments. A.P. and L.M.C. designed, performed and analysed experiments in MMTV-PyMT mice (OHSU cohort). S.T., L.L. and C.E.L designed, performed and analysed the zebrafish experiments. M.L.I.-A. designed and performed some experiments while on sabbatical in M.D.P.'s laboratory. L.M.S., A.B. and R.K.J. provided clinical samples and discussed and interpreted the results. All authors provided intellectual input, reviewed the data and the manuscript. M.D.P. designed, supervised and coordinated research, interpreted the data and wrote the manuscript.

Competing interests

L.M.S. reports consulting fees from Novartis. L.M.C. is a paid consultant for Cell Signaling Technologies, received reagent support from Plexxikon and NanoString Technologies and is a member of the Scientific Advisory Boards of Syndax Pharmaceuticals, Carisma Therapeutics and Verseau Therapeutics. A.B. reports consulting fees from Genentech/Roche, Immunomedics, Novartis, Pfizer, Merck, Radius Health, Spectrum Pharma and Taiho Pharma and received a research grant from Biothernostics. R.K.J. received honoraria from Amgen and consultancy fees from Merck, Ophthotech, Pfizer, SPARC, SynDevRx, and XTuit, owns equity in Enlight, Ophthotech, SynDevRx and serves on the Boards of Trustees of Tekla Healthcare Investors, Tekla Life Sciences Investors, Tekla Healthcare Opportunities Fund and Tekla World Healthcare Fund. M.D.P. reports honoraria from Merck and Sanofi/Regeneron Pharmaceuticals, received sponsored research grants from Hoffmann La-Roche, MedImmune and Deciphera Pharmaceuticals and serves on the Scientific Advisory Boards of Deciphera Pharmaceuticals and Genenta. The other authors declare no competing interests. Neither materials nor funding from the above organizations were used in this study.

Additional information

Supplementary information is available for this paper at https://doi.org/10.1038/s41556-018-0256-3.

Reprints and permissions information is available at www.nature.com/reprints.

Correspondence and requests for materials should be addressed to I.K. or M.D.P.

Publisher's note: Springer Nature remains neutral with regard to jurisdictional claims in published maps and institutional affiliations.

© The Author(s), under exclusive licence to Springer Nature Limited 2018

Methods

Mice. FVB/n, Balb/c, C57BL/6 and Swiss nu/nu mice were purchased from Charles River Laboratories. *Ccr2*-KO mice (C57BL/6 background) were obtained from The Jackson Laboratory (https://www.jax.org) and bred under standard conditions at the University of Edinburgh. *Rag1*$^{-/-}$ mice (C57BL/6 background) were available in the EPFL mouse facility. Transgenic MMTV-PyMT mice (FVB/n background) were available in both the EPFL mouse facility and Department of Comparative Medicine barrier facility. Male mice heterozygous for the polyoma virus middle T Antigen (PyMT) were bred with wild-type females; pups were genotyped by Transnetyx (http://www.transnetyx.com). All of the mice employed in this study were maintained in pathogen-free barrier animal facilities in accord with state regulations for the care and use of mice in experimental research.

The studies involving mice were compliant with all relevant ethical regulations regarding animal research. Most of the experiments were performed at EPFL; some experiments were performed at the University of Edinburgh (*Ccr2*-KO mice) and at Oregon Health and Science University (OHSU), Portland (MMTV-PyMT mice, *partim*). All procedures were performed according to protocols approved by the veterinary authorities of the Canton Vaud according to the Swiss Law (licences 2577, 2577.1 and 2916), the UK Animal Scientific Procedures Act (1986) licence (PPL 70/8065), the US Public Health Service, the Office for the Protection from Research Risks A-3304-01, the US Department of Agriculture 92-R-001 and the Association for Assessment and Accreditation of Laboratory Animal Care (AAALAC) International. The OHSU maintains AAALAC International accreditation and OLAW assurance (A3304-01) and all procedures with small animals at OHSU were IACUC approved (IS00001484).

Cell lines. The mouse cell lines 4T1 (mammary adenocarcinoma; ATCC), bEnd.3 (brain endothelial cells; provided by F. Bussolino, University of Turin), 293T (provided by L. Naldini, San Raffaele Scientific Institute) and PyMT-IK1 (mammary adenocarcinoma; isolated in the De Palma's lab) were maintained in Iscove's modified Dulbecco's medium (IMDM, Sigma) supplemented with 10% fetal bovine serum (FBS; Gibco), l -glutamine (Amimed) and penicillin/streptomycin (Gibco). The PyMT-IK1 cell line was isolated from a primary mammary tumour of a 14-week-old, transgenic MMTV-PyMT female mouse. Mouse E0771-LG cells (mammary adenocarcinoma; derived from the parental cell line E0771), both unmodified and stably transfected with a firefly luciferase cDNA for in vivo bioluminescence imaging (E0771-LG:Fl; both provided by T. Kitamura, University of Edinburgh)[49,58], were maintained in Dulbecco's medium (DMEM, Gibco) with 10% FBS, l -glutamine and penicillin/streptomycin. The human cell line MDA-MB-231 (breast adenocarcinoma; ATCC) was cultured in RPMI 1640 (Gibco) with 10% FBS and penicillin/streptomycin. The human melanoma cell line MDA-MB-435, which was stably transfected to express CFP (provided by R. Klemke, University of Sheffield), was maintained in DMEM with 10% fetal calf serum (BioWhittaker) and 50 μg ml^{-1} G418 (Sigma) to maintain CFP expression. All cell lines used tested negative for *Mycoplasma* contamination.

Primary cell cultures. Bone marrow dendritic cells (BMDCs) were obtained by flushing the long bones of 6-week-old C57BL/6 mice, as described previously[29], and cultured for six days in RPMI 1640 medium with 10% FBS, l -glutamine, penicillin/streptomycin and granulocyte-macrophage colony-stimulating factor (100 ng ml^{-1}; Peprotech).

Mouse embryonic fibroblasts (MEFs) were obtained from C57BL/6 mice on embryonic day 14.5 (E14.5), as described previously[59], and cultured in DMEM with 10% FBS, l -glutamine, penicillin/streptomycin. We verified the purity of MEFs (CD45$^-$CD31$^-$EpCAM$^-$CD140a$^+$) by FACS.

To obtain MMTV-PyMT tumour-derived cells, primary mammary tumours of 14-week-old female MMTV-PyMT mice were dissected, minced and digested with collagenase IV (0.2 mg ml^{-1}, Worthington), dispase (2 mg ml^{-1}; Life Technologies) and DNase I (0.002 mg ml^{-1}; Life Technologies) in IMDM medium for 30 min at 37 °C. The cell suspensions were filtered using a cell strainer (70 μm) before plating. Tumour-derived cells were then cultured for 48 h in IMDM supplemented with 5% EV-depleted FBS, l -glutamine and penicillin/streptomycin before intraveneous injection in tumour-free mice.

The treatment of primary cells with chemotherapeutic drugs was conducted in complete medium supplemented with EV-depleted, 5% FBS for three days. At the end of the treatment, the viability of BMDCs and MEFs was assessed by trypan blue staining and WST-1 assays, respectively.

Generation, production and use of lentiviral vectors. Lentiviral vectors (LVs) that express a CD9.mCherry fusion protein or human HER2 were described previously[29,60]. To disrupt *Rab27a*, *Rela* or *Anxa6* in bEnd.3 or 4T1 cells, we generated self-inducible CRISPR–Cas9-based LVs as described previously[29]. Briefly, we annealed and ligated the DNA sequences shown below using the BsmBI restriction site in the U6-(sgRNA).TetO-CAS9.hPGK-PURO/2 A/rtTA LV (ref. [29]): *Rab27a* sense, ACCGTATCCAGTTTCGGACATTG; *Rab27a* antisense, AAACCAATGTCCGAAACTGGATA; *Rela* sense, ACCGGGCTGGGGTCGGCGTACGG; *Rela* antisense, AAACCCGTACGCCGACCCCAGCC; *Anxa6* sense, ACCGGATTCCAGGTCTCGCTCAT and *Anxa6* antisense, AAACATGAGCGAGACCTGGAATC.

To generate the NF-kB reporter LV, we isolated the minimal mouse *Fos* promoter element and three copies of the major histocompatibility complex class I KB element (TGGGGATTCCCCA) by digesting a plasmid obtained from Addgene (https://www.addgene.org/26699/) with HincII and PvuII restriction enzymes. The sequence was then inserted downstream to the minimal cytomegalovirus promoter (mCMV) of a bidirectional hPGK.GFP/mCMV.mCh LV after digestion with EcoRV.

Vesicular stomatitis virus-pseudotyped, third-generation LVs were produced by transient four-plasmid co-transfection into 293T cells and concentrated by ultracentrifugation, as described previously[61]. The expression titres of LVs encoding fluorescent proteins were determined in 293T cells by limiting dilution. The LV stocks were stored at −80 °C.

PyMT-IK1 and 4T1 cells were transduced with LVs expressing CD9.mCh; 4T1-mCh cells were further transduced with a HER2-expressing LV for use in some experiments. Cells expressing HER2 and/or mCh were sorted by FACS (Aria II apparatus, BD Biosciences) to establish pure cell populations expressing the transgene(s) of interest.

To disrupt *Rab27a*, *Rela* or *Anxa6*, bEnd.3 and 4T1-mCh cells were transduced with CRISPR–Cas9 LVs. After transduction, the cells were cultured in complete IMDM medium with puromycin (5–10 μg ml^{-1}; Sigma) and doxycycline (10 μg ml^{-1}; Sigma) for four days to select transduced cells. The cells were then plated in normal medium to isolate cell clones. Cell colonies that showed no expression of RAB27A, RELA or ANXA6 by western blotting were expanded and employed in further experiments.

Cytotoxic drugs. PTX dissolved in CREMO (Labatec) was obtained at a stock concentration of 6 mg ml^{-1}. PTX was used at 100 ng ml^{-1} (cell culture experiments), 10 mg kg^{-1} (mouse models) or 100 nM (zebrafish models), unless indicated otherwise. CREMO (Sigma) was used as a control vehicle for PTX, both in vitro and in vivo. Oregon Green-488-conjugated PTX (Thermo Fisher Scientific) was reconstituted in DMSO and used at a concentration of 100 ng ml^{-1}. Docetaxel (Sigma) and DOX (adriblastine; Pfizer) were reconstituted in DMSO, whereas gemcitabine (Sigma) was reconstituted in water. Unless indicated otherwise, DOX, docetaxel and gemcitabine were used in cell culture experiments at 200, 100 and 10 ng ml^{-1}, respectively. For mouse studies, DOX was dissolved in PBS and used at 8 mg kg^{-1}.

Cytotoxic drugs (or control vehicle) were added once to the cell culture medium and the experiments terminated after 24 to 72 h. The mice received three doses of either PTX or DOX, as described below.

Treatment of transgenic MMTV-PyMT mice. Female transgenic mice were treated with 10 mg kg^{-1} PTX or CREMO in PBS administered either intraperitoneally (EPFL cohort) or intraveneously (OHSU cohort), or 8 mg kg^{-1} DOX or PBS administered intraperitoneally. All of the mice received three drug/vehicle doses at five-(PTX) or seven-day (DOX) intervals, starting at 11–12 weeks of age, when multifocal mammary tumours were evident in this model[46]. The mice were euthanized three days after the last dose. Tumour weight measurements were performed at necropsy by dissecting the ten mammary glands.

Treatment of mice carrying subcutaneous tumours. Subcutaneous 4T1 tumours were established by implanting 4T1, 4T1-mCh or 4T1-mCh/HER2 cells (10^6 × cells) in the right flank of 6- to 8-week-old Balb/c, *Rag1*$^{-/-}$ or Swiss nu/nu mice. Both female and male *Rag1*$^{-/-}$ mice were employed; only female Balb/c and Swiss nu/nu mice were employed. Treatments were initiated when the tumour volume reached 100–200 mm^3; the mice were euthanized three days after the last drug dose. Tumour growth was monitored twice a week and the tumour size determined by caliper measurements. The tumour volume was calculated using the formula: tumour volume (mm^3) = (length (mm)) × (width (mm)) × (height (mm)) × 0.5236. The tumour weight measurements were performed at necropsy.

Isolation of EVs from media conditioned by continuous and primary cell cultures. To isolate EVs, cells were cultured and expanded in the appropriate medium. When the cells were at about 40–50% confluence, they were moved to medium containing 5% EV-depleted FBS, which was obtained by ultracentrifugation of standard FBS at 134,000 *g* for 16 h at 4 °C followed by filtration through a 0.1 μm vacuum filtration bottle. EVs were isolated from the conditioned medium using sequential ultracentrifugation, as previously described[29,30]. Briefly, conditioned medium was centrifuged at 500*g* for 5 min, 2,000 *g* for 10 min and 4,600 g for 20 min at 4 °C to remove dead cells and debris. The medium was then ultracentrifuged at 134,000 *g* for 70 min at 4 °C using a Beckman ultracentrifuge and SW32Ti rotor. The pellet was washed in 35 ml PBS and ultracentrifuged again at 134,000 g for 70 min at 4 °C. The resulting EV preparation was dissolved in either PBS or RIPA buffer (Sigma), depending on the application, and either used immediately or stored at −80 °C. The average EV yield obtained from 4T1, PyMT-IK1, MDA-MD-231, E0771-LG, BMDCs and MEFs was 7.3, 0.8, 0.8, 1.8, 0.1 and 1 μg (determined by BCA) per ml of cell culture medium, respectively.

Isolation of MMTV-PyMT tumour-derived EVs. After treatment of the mice with cytotoxic drugs, primary MMTV-PyMT tumours were made into single cell suspensions as described above. The tumour-derived cells were cultured for 48 h in IMDM supplemented with 5% EV-depleted FBS, l -glutamine and penicillin/streptomycin before EV isolation by ultracentrifugation. The average yield of purified EVs was 50 μg per gram of tumour.

Isolation of EVs from mouse or human plasma. We obtained blood from 4T1-mCh tumour-bearing mice treated with PTX or CREMO by cardiac puncture after deep sedation (150 mg kg^{-1} pentobarbital administered intraperitoneally). To obtain plasma for EV isolation or mCh quantification, blood was centrifuged at 500 g for 5 min, 2,000*g* for 15 min and 10,000*g* for 20 min at 4 °C to remove cells, debris and large vesicles. Human plasma was obtained as described below.

To isolate EVs, plasma was ultracentrifuged at 134,000 g for 70 min at 4 °C using a Beckman ultracentrifuge and SW55Ti rotor. The pellet was washed in 4.5 ml PBS and ultracentrifuged again at 134,000 g for 70 min at 4 °C. The resulting EV preparation was dissolved in PBS and either used immediately or stored at −80 °C.

Quantification of EVs. EV preparations were analysed for protein content using the BCA protein assay reagent kit (Thermo Fisher Scientific). The size and concentration of EVs were determined by NTA using a Nanosight NS300 device (Malvern Instruments). We tested different sample dilutions (1:50 to 1:2,000 in PBS) whereby particle concentration was within the optimal range of detection (5×10^7–1×10^9 particles ml^{-1}). All of the camera settings were set at the beginning of the session and kept fixed during all of the acquisitions in a given experiment: camera level, 7–9; camera gain, 10–12; detection threshold, 2–4. For each sample, at least three videos of 60 s for at least one EV dilution were taken and analysed using the NTA software 3.0 with default settings.

TEM of purified EVs. Purified EVs (5 μg in 15 μl PBS) were applied to carbon-coated 400 mesh grids (Electron Microscopy Sciences) for 5 min, then washed with PBS and stained with 2% uranyl acetate for 30 s, as described previously[62]. Images were obtained using a TEM device (Tecnai Spirit, FEI Company).

Sucrose gradient fractionation of EVs. Purified EVs were subjected to continuous sucrose gradient fractionation using established procedures[31,63]. Briefly, 12 stock solutions with decreasing sucrose concentrations were layered on top of purified EVs (800 μg in 100 μl PBS) in a total volume of 12 ml, followed by ultracentrifugation at 100,000 g for 16 h at 4 °C with a Beckman ultracentrifuge and a SW40Ti rotor. Six fractions (2 ml each) were then collected and transferred to new tubes; the density of each sucrose fraction was measured using a refractometer. Each fraction was washed with 10 ml PBS and ultracentrifuged at 110,000 g for 70 min at 4 °C as above. EVs were resuspended in 100 μl PBS previous to subsequent analyses.

Quantification of EV-associated mCh fluorescence in cell culture media and mouse plasma. The fluorescence of mCh was measured in 100 μl PBS containing purified EVs or 100 μl mouse plasma, using a spectrophotometer (Infinite2000 plate-reader, TECAN). The following parameters were used: excitation wavelength, 586 nm; emission wavelength, 625 nm and four reads.

To degrade free (non-EV-associated) mCh protein, a proteinase K reaction was performed using 40% plasma and 0.25 mg ml^{-1} proteinase K (Promega) in 1 mM guanidinium hydroxide, 30 mM Tris and 5 mM $CaCl_2$ for 2 h at 55 °C.

Determination of PTX and DOX concentration in EVs. The content of PTX and DOX in purified EVs was assessed by measuring the fluorescence intensity of Oregon Green-488-conjugated PTX (Thermo Fisher Scientific) and the spontaneous fluorescence of DOX (Sigma), respectively, using a spectrophotometer (TECAN infinite2000 plate-reader). We measured several dilutions of the EVs in PBS, as well as equal amounts of drug-free EVs from DMSO-treated cells for background subtraction. The following parameters were utilized for measuring the fluorescence of Oregon Green-488-conjugated PTX and DOX, respectively: excitation wavelengths, 495 and 470 nm; emission wavelengths, 525 and 585 nm and four reads per EV dilution for both. Standard curves of Oregon Green-488-PTX and DOX were employed to extrapolate the drug concentration in EVs from fluorescence intensity values.

EV pre-conditioning of mice. Cell- or tumour-derived EVs (15 μg in 100 μl PBS) were centrifugated at 4,600 g for 1 min at 4°C to remove sedimentable aggregates before intravenous injection into 6- to 8-week-old, tumour-free mice (FVB/n, C57BL/6/*Rag1*$^{-/-}$, Balb/c, C57BL/6/*Ccr2*-KO or C57BL/6). Two EV doses were administered two days apart. For gene expression and FACS analyses, tumour-free mice were euthanized two days after the last EV dose. For experimental metastasis (lung colonization) studies, cancer cells were infused intravenously one day after the last EV administration and euthanized at the time points described below.

Lung colonization studies. Six- to eight-week-old male or female *Rag1*$^{-/-}$ mice were intravenously injected with 5×10^5 4T1-mCh cells one day after EV pre-conditioning. The mice were euthanized three weeks after the cancer cell injection and their lungs were fixed, sectioned and analysed for direct mCh fluorescence to quantify the metastatic tumour burden.

Six-week-old female Balb/c mice were intravenously injected with 1×10^5 4T1 cells one day after EV pre-conditioning. The mice were euthanized ten days after the cancer cell injection and their lungs wer fixed, sectioned and stained with hematoxylin and eosin (H&E) to quantify the metastatic tumour burden.

MMTV-PyMT tumour-derived cells (5×10^5) were intravenously injected into 6–7-week-old female FVB/n mice one day after EV pre-conditioning. The mice were euthanized three weeks after the tumour cell injection and their lungs were fixed, sectioned and stained with H&E to quantify the metastatic tumour burden.

E0771-LG:Fl cells (1×10^6) were intravenously injected into 6–8-week-old male or female C57BL/6 or C57BL/6/*Ccr2*-KO mice one day after EV pre-conditioning. Bioluminescence was determined ten days after the cancer cell injection.

In vivo bioluminescence imaging. C57BL/6 or *Ccr2*-KO mice were anaesthetised with isofluorane (3–4% induction, 1–2% maintenance), and administered 150 μ g luciferin (GoldBio) intraperitoneally per gram of body weight. The mice were imaged under a Photon Imager Optima (Biospace Lab) for 15 min until the bioluminescence signal reached a plateau. The imaging was conducted at both 30 min and ten days after E0771-LG:Fl cell injection. Photon counts (photon s^{-1} cm^{-2} sr^{-1}) in the lung area were analysed using the M3 Vision software (Biospace Lab).

Analysis of pulmonary metastasis in mice. To analyse lungs for the presence of mCh-negative tumour nodules, formalin- or paraformaldehyde-fixed lungs were sectioned into 5-μm- and 8-μm-thick sections, respectively, at 100 μm intervals. Three to four large lung sections were stained with H&E. The sections were scanned with an Olympus slide scanner (VS120-L100) endowed with a × 10 objective and fully automated scanning capabilities. Tumour nodules (>10–20 cancer cells) were counted and their area measured using the OlyVIA (Olympus) and ImageJ softwares, respectively. The number and mean area of the metastatic nodules were calculated by averaging data from individual sections.

To analyse lungs for the presence of mCh^+ tumour nodules or disseminated cancer cells, paraformaldehyde-fixed lungs were sectioned into 8-μm-thick sections at 100 μm intervals. Four large sections were counterstained with DAPI and scanned with an Olympus slide scanner (VS120-L100) to acquire both mCh and DAPI fluorescence. The images were analysed using the ImageJ software and the VSI Biop tool. The total metastatic area was calculated by normalizing the mCh^+ area to the total lung ($DAPI^+$) area and by averaging data from individual sections. In some experiments, mCh^+ cancer cells were also quantified by FACS analysis of homogenised lung tissue.

Zebrafish studies. The studies involving zebrafish (*Danio rerio*) were compliant with all relevant ethical regulations regarding animal research. The zebrafish were maintained according to standard protocols. All tumour studies were authorised by the UK Home Office under licence 40/3690 and performed at the zebrafish facility of the University of Sheffield. The transgenic zebrafish line *fms*:UNM[64] was crossed with the Tg(tie2:GFP) line[65] to obtain the double transgenic *fms*:UNM; Tg(tie2:GFP) line, which enables the direct visualization of blood and lymphatic vessels.

Zebrafish embryos were maintained in E3 medium at 28 °C. Before injection of EVs (or free drug) and cancer cells, embryos (56 h post-fertilization) were anaesthetised by immersion in 0.04 mg ml^{-1} tricaine (MS222; Sigma) and immobilized in 1% low melting point agarose (Sigma). Each embryo received 200–300 CFP^+ MDA-MB-435 cells together with purified EVs (0.326 μg ml^{-1}) or drugs (PTX or CREMO; 100 μM) in 4 nl saline via the duct of Cuvier with a microinjector (World Precision Instruments).

The embryos were analysed 18 h post-injection. After anaesthesia/immobilization, we used a spinning disc confocal microscope (Olympus IX81, PerkinElmer) to image the tail of the zebrafish and capture *Z* -stacks at 3 μ m increments. The full tail of the embryo was covered by two images at ×10 magnification. Image acquisition and processing were performed with Volocity 6.3 software (Improvision). Cancer cell aggregates were visualized by capturing the CFP fluorescence of the cells and the total metastatic volume was calculated from the XYZ analysis of CFP fluorescence in each of the tumour *Z*-stacks.

Preparation of tumours, lungs and livers for FACS analysis and cell sorting. Before euthanization, deeply anaesthetised mice were perfused with PBS to remove intravascular blood cells. Tumours, lungs and livers were then harvested, washed extensively in PBS and then minced before digestion with collagenase IV (0.2 mg ml^{-1}), dispase (2 mg ml^{-1}) and DNase I (0.002 mg ml^{-1}) in IMDM medium for 20 min at 37 °C. The cell suspensions were filtered using a cell strainer (70 μ m) and washed in PBS containing 2 mM EDTA and 2% FBS. Red blood cells were lysed using a Red blood cell Lysis buffer (Sigma).

Cell suspensions were incubated with rat anti-mouse FcγIII/II receptor (CD16/CD32) blocking antibodies (4 μg ml^{-1}) for 15 min at 4 °C previous to extracellular staining with conjugated antibodies (Supplementary Table 4) for 20 min at 4 °C. Before analysis, cells were resuspended in DAPI-containing buffer to identify

non-viable cells. All of the samples were analysed using an LSRII apparatus (BD Biosciences). Compensation was performed using FMO controls.

To sort cells, we used a FACS Aria II apparatus (BD Biosciences). Each cell population was isolated from a single organ/mouse. Typically, 2×10^3 to 2×10^5 cells were obtained from each sorting session and all populations were verified by performing post-sorting analysis. Cell types were identified using the following combinations of cell markers: ECs, CD45$^-$CD31$^+$; Ly6C$^+$ classical monocytes, CD45$^+$CD11b$^+$Ly6C$^+$Ly6G$^-$F4/80$^+$; Ly6C^{low} monocytes, CD45$^+$CD11b$^+$Ly6C^{low}Ly6G$^-$F4/80$^-$; monocytes/macrophages, CD45$^+$CD11b$^+$Gr1$^-$ or CD45$^+$CD11b$^+$Ly6G$^-$Ly6C^{low}; alveolar lung macrophages, CD45$^+$CD11c$^+$SiglecF$^+$F4/80$^+$; non-alveolar lung macrophages, CD45$^+$CD11c$^-$SiglecF$^-$CD11b$^+$Ly6G$^-$Ly6C^{low}F4/80$^+$; neutrophils, CD45$^+$CD11b$^+$Ly6G$^+$ and disseminated cancer cells, CD45$^-$CD31$^-$mCh$^+$.

Quantification of circulating cancer cells by FACS. Blood was collected by cardiac puncture of deeply anaesthetised mice and collected in EDTA-containing tubes. To enumerate the circulating cancer cells, we used 250 µl erythrocyte-depleted blood. The cell suspension was processed as described above and the circulating cancer cells were identified as CD45$^-$mCh$^+$HER2$^+$ cells using an LSRII apparatus.

Immunofluorescence staining of tumour and organ sections. Tumours and organs were fixed in 4% paraformaldehyde for 24 h at 4 °C, equilibrated in sucrose solutions for 24 h and then embedded in optimal cutting temperature (O.C.T) compound (Cryomatrix, Thermo Fisher Scientific) on dry ice with iso-pentane (VWR Chemicals) before storage at −80 °C. Tissue sections of 8 µm were obtained using a Leica cryostat CM1950 (Leica Biosystems). Before staining, the sections were rehydrated and then incubated with blocking solution (1% BSA, 10% FBS, 0.3% Triton X-100 and rat anti-mouse FcγII/III receptor (1:100) in PBS) for 1 h at room temperature. The sections were incubated overnight at 4 °C in 100–200 µl blocking solution containing the primary antibodies listed in Supplementary Table 4. Non-conjugated antibodies were revealed with secondary antibodies. After staining, the nuclei were labelled with DAPI (1 µg ml^{-1}) and sections mounted in Dako fluorescence mounting medium, covered with cover glass (Heathrow Scientific) and stored at 4 °C.

Immunofluorescence staining of cultured cells. Cells were seeded on glass chamber slides (Lab-Tek) or glass coverslips (Electron Microscopy Sciences) coated with 50 µg ml^{-1} poly-L-lysine (Sigma). After 16–24 h, the cells were treated with drugs or EVs for an additional 24 h. At the time of analysis, the cells were washed with PBS, fixed with 4% paraformaldehyde for 20 min, permeabilised with a solution containing 0.1% Triton X-100 in PBS for 10 min and blocked with 1% BSA in PBS for 1 h at room temperature. Primary antibodies (Supplementary Table 4) were then applied overnight at 4 °C. In some experiments, Alexa Fluor-488 Phalloidin (1:40; Life Technologies) was added to label the actin cytoskeleton. The slides were washed and secondary antibodies applied for 1 h in blocking solution at a final dilution of 1:200. After washing, the cell nuclei were labelled with DAPI (1 µ g ml^{-1}) or DRAQ5 (20 µM; Thermo Fisher Scientific) and the slides mounted.

Duolink staining. Cells (bEnd.3) were seeded on poly-L-lysine-coated glass coverslips in a 48-well plate and incubated for 24 h with PBS, CREMO- or PTX-EVs (50 µg ml^{-1}) from 4T1 cells. The cells were then washed with PBS and fixed with 4% paraformaldehyde for 20 min. After several washes with PBS, cells were permeabilised with 0.3% Triton for 20 min. The Duolink PLA technology (Sigma) was then applied to examine physical proximity between ANXA6 and p65. Specifically, the Red starter kit mouse/rabbit was used according to the manufacturer's instructions. The primary rabbit anti-ANXA6 (Life Technologies, 720161) and mouse anti-p65 (clone F-6; Santa Cruz, sc-8008) antibodies were incubated overnight at 1:400 and 1:150, respectively, together with Alexa Fluor-488 Phalloidin (1:40; Life Technologies) to label the actin cytoskeleton.

Image acquisition by confocal microscopy. To image immunostained tissue sections and cultured cells, we used a Zeiss LSM700 confocal microscope coupled to a high sensitivity Axiocam MRm (B/W) camera. Fluorescent signals from individual fluorophores were acquired sequentially from single optical sections, analysed and pseudocoloured using the ZEN software (Zeiss) or ImageJ.

Subcellular localization of mCh by immunofluorescence staining and confocal microscopy. To determine the subcellular localization of mCh in 4T1-mCh cultures exposed to drugs, confocal images were analysed using the ImageJ software. For each cell, the lining of the plasma membrane (±0.5 µm) was determined manually by visualizing beta-tubulin immunostaining and saved as a region of interest, whereas the lining of the nucleus was determined according to DAPI staining by applying a Yen threshold with the Analyze particle tool of ImageJ. The cytoplasmic area was defined as the area between the plasma membrane and the nucleus. The signal intensity of mCh was calculated in both plasma membrane and cytoplasm compartments, and expressed as a ratio.

Quantification of mCh and ANXA6 transfer to ECs. To study mCh transfer, bEnd.3 cells were seeded in 24-well plates either directly on the plastic (for FACS and western blotting) or on poly-l -lysine-coated glass coverslips (for immunofluorescence staining). The cells were then treated with purified EVs (1–200 µg ml^{-1} total protein) or medium conditioned by cultured cancer cells. Before use, the conditioned medium was centrifuged at 500 g for 5 min, 2,000 g for 5 min and 4,600 g for 20 min at 4 °C to remove dead cells, debris and large vesicles. The bEnd.3 cells were then allowed to grow for additional 24 h before analysis. Immediately before analysis, the cells were extensively washed with PBS and treated with trypsin/EDTA to detach them (FACS), lysed with RIPA buffer or fixed with paraformaldehyde (immunofluorescence staining).

Chemicals and cytokines. Cas-BIND Pro Pan Caspase Pro-VAD-FMK (Verget Bioscience) or control DMSO were added to 40–50% confluent cells at a final concentration of 10 µM in EV-depleted medium. After 2 h, PTX (100 ng ml^{-1}) or CREMO were added for another 72 h. The cell permeant chelator BAPTA-AM (Life Technologies) or control DMSO were added to 40–50% confluent cells to a final concentration of 3 µM in EV-depleted medium. After 2 h, PBS, PTX (100 ng ml^{-1}), DOX (200 ng ml^{-1}) or the appropriate vehicle were applied for a further 48 h. Recombinant human TNFα was purchased from Peprotech and used at 20 ng ml^{-1} in complete growth medium.

Cell viability and apoptosis assays. Cell viability was assessed using a WST-1 assay (Roche) according to the manufacturer's instructions. Briefly, 5,000 cells were seeded in 96-well plates and treated with drugs as described above. After 72 h, 10 µ l WST-1 reagent was added to each well and absorbance at 450 nm was measured using a TECAN plate-reader.

Cell apoptosis was assessed by FACS analysis of biotin-conjugated annexin V (BD Biosciences) and 7AAD (Sigma), according to the manufacturer's instructions. Briefly, 200,000 cells were seeded in 6-well plates and treated with drugs. After 48 h, the cells were trypsinized and transferred to a tube along with the conditioned medium. The cells were centrifuged at 2,000 r.p.m., washed with ice-cold PBS and resuspended in 1×binding buffer at a concentration of 10^6 cells ml^{-1}. The cell suspension was then stained with biotin-conjugated annexin V for 15 min at room temperature followed by streptavidin-eFluor 450 (1:100; eBioscience) for 15 min on ice. After washing, the cells were resuspended in 7AAD (1:200) and immediately analysed by FACS.

Gene expression analyses by quantitative PCR. Small tissue fragments were obtained from the lungs of perfused tumour-free or bearing mice, washed in PBS, frozen on dry ice and stored at −80 °C. Total RNA was purified using the miRNeasy mini kit guidelines (Qiagen). RNA was quantified with a NanoDrop ND-2000 and retrotranscribed using a SuperScript Vilo cDNA synthesis kit (Invitrogen).

All quantitative PCR (qPCR) reactions were performed using the following TaqMan gene assays: *Hprt* Mm 01545399-m1, *B2m* Mm 00437762_m1, *Gapdh* Mm99999915_g1 *Angpt2* Mm00545822_m1, *Csf1* Mm00432686_m1, *Il6* Mm00446190_m1, *Cxcl12* Mm 00445553-m1, *Ccr2* Mm04207877_m1 and *Ccl2* Mm00441242 (Applied Biosystems/Life Technologies). Each assay was performed in three technical replicates using 10 ng total cDNA per reaction and 2× TaqMAN Universal master mix (Life Technologies). Quantitative PCR reactions were performed for 40 cycles in standard mode using an ABI7900HT apparatus (Applied Biosystems). Raw data were extracted and evaluated using the SDS software v2.4. For the analysis of results, we calculated the average of the median threshold cycle (C_t) of one or two reference genes (*Hprt*, *Gapdh* and/or *B2m*) for each sample (reference C_t), as described previously[66].

Western blotting. Cells or purified EVs were lysed in ice-cold RIPA buffer containing Halt protease and phosphatase inhibitors (Thermo Fisher Scientific). Conditioned medium was concentrated using Vivaspin 20 columns (5,000 molecular weight (MW) cutoff; Sartorius). Protein concentrations were determined using the BCA protein assay reagent kit (Thermo Fisher Scientific). The proteins were denatured at 95 °C for 5 min with 6×Laemmli buffer (Bioworld) or at 90 °C for 10 min with 4×LDS Sample buffer and 10×Reducing agent (Life Technologies). Unless stated otherwise, matched protein amounts for each sample were analysed in each experiment.

Proteins (10 to 20 µg) were separated by 12% or 4–12% (gradient) SDS–PAGE (Life Technologies) and blotted onto PVDF membranes (Amersham Hybond 0.45 µm; GE Healthcare). The membranes were blocked with 5% milk in tris-buffered saline-Tween 20 (TBS-T) for 24 h, incubated with primary antibodies (Supplementary Table 4) for 12 h at 4 °C and then with horseradish peroxidase (HRP)-conjugated secondary antibodies for 1 h at room temperature. The proteins of interest were visualized using the ECL western blotting substrate (Pierce) and a Fusion FX7 device (Peqlab). In some experiments, the PVDF membranes were instead blocked with Odyssey blocking buffer (LI-COR Biosciences), incubated with primary antibodies for 12 h at 4 °C followed by IRDye 800CW or 680RD-conjugated secondary antibodies (LI-COR Biosciences) in 0.1% Tween and 0.01% SDS for 1 h at room temperature. The blots were imaged on the LI-COR Odyssey scanner.

ELISA. After dissection, lungs were immediately frozen on dry ice and stored at −80 °C. For protein extractions, lungs were washed with ice-cold PBS and minced

into small fragments before mechanical homogenization in PBS containing Halt phosphatase and protease inhibitors (Thermo Fisher Scientific). After three freeze–thaw cycles to break cellular membranes, the homogenates were centrifuged at 13,000 r.p.m. for 15 min at 4 °C. To measure CCL2, we used the Quantikine mouse/rat CCL2/MCP-1 immunoassay kit from R&D (MJE00) and 50 mg total protein for each reaction. Enzyme-linked immunosorbent assay (ELISA) was performed according to the manufacturer's instructions. Absorbance was measured using a TECAN Safire2 plate-reader.

To examine if ANXA6 localizes on the EV surface, we used a homemade ELISA and a polyclonal anti-ANXA6 antibody (Thermo Fisher Scientific, 720161). Antibodies against the endoplasmic reticulum protein GP96 (clone 9G10; Enzo) or the extracellular domain of CD81 (clone B-11; Santa Cruz) were used as negative and positive controls, respectively, to stain the outer EV surface. The antibodies were diluted (5 μg ml^{-1}) in ELISA coating solution (Thermo Fisher Scientific) and used for coating a Nunc MaxiSorp 96-well plate (Thermo Fisher Scientific). The plate was then blocked with ELISA blocking solution (Thermo Fisher Scientific) and washed (two washes with PBS containing 0.04% Tween followed by two washes with only PBS) before EVs (150 μg ml^{-1} in PBS) were added and incubated overnight at 4 °C. A TECAN Safire2 plate-reader was used for the acquisition of EV-associated mCh fluorescence, before and after four washes with PBS to remove unadsorbed EVs. A final acquisition was performed after the EVs were lysed with 0.3% Triton in PBS for 2 h at 4 °C and three PBS washes.

EDTA treatment of EVs. To examine the localization of ANXA6 in EVs, EVs were treated with PBS or EDTA in PBS (1 mM) for 30 min at 37 °C. After three washes with PBS, the EVs were loaded onto Vivaspin 500 columns (300,000 MW cutoff; Sartorius) and centrifuged at 4,000 g for 15 min to retain the EVs and discharge free macromolecules, before western blot analysis.

Late endosome enrichment. Cells were treated with drugs for 24 h. After cell homogenization with a 25-gauge needle, we enriched the late endosomes through continuous density gradient centrifugation[67]. The 25%/homogenization buffer (HB), enriched in late endosomes, and 35%/40.6%, enriched in heavier membranes (for example, endoplasmic reticulum and mitochondria), interfaces were collected and concentrated by ultracentrifugation (100,000*g* for 1 h) using a Beckman ultracentrifuge. The 40.6% fraction enriched in cytosolic proteins was also collected to concentrate proteins with Vivaspin 20 columns (3,000 MW cutoff; Sartorius).

NF-kB reporter assay. Cells were transduced with the NF-kB reporter LV and treated with 10 μg ml^{-1} EVs several weeks after transduction. Two days post-EV treatment, the cells were trypsinized, washed in EDTA and analysed by FACS. To quantitate NF-kB activity, we calculated the fluorescence intensity of both green fluorescent protein (GFP) and mCh after subtracting the background fluorescence of untransduced cells. In studies involving PTX-EVs, NF-kB activity was determined as the ratio between mCh and GFP fluorescence. In studies involving DOX-EVs, NF-kB activity was determined from GFP fluorescence, as DOX is fluorescent in the red channel.

LC–MS/MS. The EVs (17 μg) of PTX- or CREMO-treated 4T1 cells were directly analysed by LC–MS/MS. EV-derived proteins of MDA-MB-231 cells (1 μg) or human plasma (1 μg) were first resolved on a denaturing 4–12% polyacrylamide gradient gel. Gel slices were excised in the area predicted to contain ANXA6 (ranging from 60 to 85 kDa) to elute proteins for LC–MS/MS.

To perform LC–MS/MS, we applied a previously published procedure[68]. Briefly, peptides were desalted using StageTips, dried in a vacuum concentrator and separated by reverse phase chromatography using a Dionex Ultimate 3000 RSLC nano UPLC system connected in-line with an Orbitrap Elite (Thermo Fisher Scientific). A database search was performed using Mascot 2.5 (Matrix Science) and SEQUEST in Proteome Discoverer v.1.4. against a murine or human Uniprot protein database. Data were further processed and inspected in ScaffoldTM 4.8.4 (Proteome Software); quantitative values normalized to total spectra were used to compare the proteomic profiles.

Plasma isolation from breast cancer patients. Using an IRB-approved sample collection protocol at the Massachusetts General Hospital Cancer Center, subjects were consented for serial venous blood collections. The study was compliant with all relevant ethical regulations regarding research involving human participants. Plasma samples were obtained from six women that were diagnosed with invasive breast cancer and with histopathologically confirmed tumour stages ranging from IA to IIIA; the immunohistochemical subtyping and lymph node status of each patient are reported in Supplementary Table 2. Blood (20 ml) was collected into Streck tubes for all subjects before initiation of neoadjuvant chemotherapy, which consisted of four cycles of dose-dense DOX at 60 mg m^{-2} and cyclophosphamide at 600 mg m^{-2} (AC) every two weeks followed by four cycles of PTX at 175 mg m^{-2} every two weeks. A second 10 ml blood sample was collected before starting PTX (on the day of the first PTX infusion) and a third 10 ml blood sample on the last or second-to-last cycle of PTX.

All blood samples were centrifuged at 1,600 g at room temperature for 10 min. The supernatant (plasma) was then transferred to a fresh 10 ml centrifuge tube without disturbing the cellular layer and centrifuged at 3,000 g at room temperature for 10 min. The supernatant from the second centrifugation was stored in 2 ml pre-labelled cryogenic vials at −70 °C. Before EV isolation, plasma was centrifuged at 10,000 g for 20 min at 4 °C; 1 ml of plasma was processed for EV isolation.

Statistics and reproducibility. The information on the study outline, sample size and statistical analysis is presented in the main text, figures and figure legends. The studies involving independent cohorts of mice were typically performed once, with the exceptions stated in the figure legends. Each study was designed to use the minimum number of mice required to obtain informative results (that is, quantitative data suited to statistical analysis) and sufficient material for further studies. No specific statistical tests were used to predetermine the sample size.

The investigators were not blinded when assessing the results or analysing data. On rare occasions, the outliers at end-point were excluded. The ROUT method (GraphPad Prism) was used to identify outliers. In rare cases, selected samples were lost or excluded from specific analyses because of technical flaws during sample collection, processing or data acquisition.

The number of biological (non-technical) replicates for each experiment is indicated in the figure legends. All of the experiments were repeated independently with similar results. When fewer than three biological replicates were available, statistics were not computed. Data are shown as mean ± s.e.m. for most analyses, with the exception of in vitro studies with a sample size of $n = 3$ for which mean ± s.d. are reported. In the experiments that involved animals, each dot in the chart represents one mouse or zebrafish embryo. The source data for all experiments are provided in Supplementary Table 5.

The statistical analysis of the data was performed using the GraphPad Prism software. Statistical analysis of differentially expressed proteins in the LC–MS/MS 4T1-EV study was performed using an unpaired two-tailed *t*-test implemented in R; *P* values were adjusted after correcting for false discovery rate using the Benjamini–Hochberg method. Unless indicated otherwise, statistical analyses of experiments that involved more than two experimental groups was conducted using one-way ANOVA with Tukey's correction for multiple comparisons. When the influence of two nominal variables on one measurement variable was examined, a two-way ANOVA followed by Tukey's or Sidak's correction was applied. Experiments that involved two experimental groups were analysed by unpaired two-tailed Student's *t*-tests with a 95% confidence interval, unless indicated otherwise.

The statistical significance of the data is summarized as follows: $^{*}P < 0.05$, $^{**}P < 0.01$, $^{***}P < 0.001$ and $^{****}P < 0.0001$. Differences between experimental groups were considered significant at *P* values lower than 0.05. Exact *P* values are provided in all instances, except when $P > 0.05$ or $P < 0.0001$.

Reporting summary. Further information on research design is available in the Nature Research Reporting Summary linked to this article.

Data availability

Uncropped and replicate western blots that are not shown in the figures are provided in Supplementary Fig 9. The 4T1-EV data have been submitted to the EV-TRACK knowledgebase (EV-TRACK ID: EV180041; ref. [69]). The mass spectrometry proteomics data have been deposited to the ProteomeXchange Consortium via the PRIDE partner repository[70] with the following dataset identifiers: PXD010362 (accession) and 10.6019/PXD010362 (DOI) for the 4T1 EV data and PXD010292 (accession) and 10.6019/PXD010292 (DOI) for the human EV data. The source data for all graphical representations are provided as Supplementary Tables 3 and 5. All other data supporting the findings of this study are available from the corresponding authors on request.

References

58. Kitamura, T. et al. Monocytes differentiate to immune suppressive precursors of metastasis-associated macrophages in mouse models of metastatic breast cancer. *Front. Immunol.* **8**, 2004 (2017).
59. Xu, J. Preparation, culture, and immortalization of mouse embryonic fibroblasts. *Curr. Protoc. Mol. Biol.* **70**, 28.1.1–28.1.8 (2005)..
60. Squadrito, M. L. et al. Endogenous RNAs modulate microRNA sorting to exosomes and transfer to acceptor cells. *Cell Rep.* **8**, 1432–1446 (2014).
61. De Palma, M. & Naldini, L. Transduction of a gene expression cassette using advanced generation lentiviral vectors. *Methods Enzymol.* **346**, 514–529 (2002).
62. Cianciaruso, C. et al. Primary human and rat beta-cells release the intracellular autoantigens gad65, ia-2, and proinsulin in exosomes together with cytokine-induced enhancers of immunity. *Diabetes* **66**, 460–473 (2017).

63. Chiou, N. -T. & Ansel, M. K. Improved exosome isolation by sucrose gradient fractionation of ultracentrifuged crude exosome pellets. *Protoc. Exch.* https://doi.org/10.1038/protex.2016.057 (2016).
64. Gray, C. et al. Simultaneous intravital imaging of macrophage and neutrophil behaviour during inflammation using a novel transgenic zebrafish. *Thromb. Haemost.* **105**, 811–819 (2011).
65. Motoike, T. et al. Universal GFP reporter for the study of vascular development. *Genesis* **28**, 75–81 (2000).
66. Keklikoglou, I. et al. Periostin limits tumor response to VEGFA inhibition. *Cell Rep.* **22**, 2530–2540 (2018).
67. de Araujo, M. E., Lamberti, G. & Huber, L. A. Isolation of early and late endosomes by density gradient centrifugation. *Cold Spring Harb. Protoc.* **2015**, 1013–10164 (2015).
68. Chopra, T. et al. Quantitative mass spectrometry reveals plasticity of metabolic networks in *Mycobacterium smegmatis*. *Mol. Cell. Proteomics* **13**, 3014–3028 (2014).